Nuclear Instruments and Methods in Physics Research A 637 (2011) 60–76

Contents lists available at ScienceDirect

Nuclear Instruments and Methods in Physics Research A

journal homepage: www.elsevier.com/locate/nima

The electron–ion scattering experiment ELISe at the International Facility for Antiproton and Ion Research (FAIR)—A conceptual design study

A.N. Antonov [a], M.K. Gaidarov [a], M.V. Ivanov [y], D.N. Kadrev [a], M. Aïche [b], G. Barreau [b], S. Czajkowski [b], B. Jurado [b], G. Belier [c], A. Chatillon [c], T. Granier [c], J. Taieb [c], D. Doré [d], A. Letourneau [d], D. Ridikas [d], E. Dupont [d], E. Berthoumieux [d], S. Panebianco [d], F. Farget [e], C. Schmitt [e], L. Audouin [f], E. Khan [f], L. Tassan-Got [f], T. Aumann [g], P. Beller [g,1], K. Boretzky [g], A. Dolinskii [g], P. Egelhof [g], H. Emling [g], B. Franzke [g], H. Geissel [g], A. Kelic-Heil [g], O. Kester [g], N. Kurz [g], Y. Litvinov [g], G. Münzenberg [g], F. Nolden [g], K.-H. Schmidt [g], Ch. Scheidenberger [g], H. Simon [g,*], M. Steck [g], H. Weick [g], J. Enders [h], N. Pietralla [h], A. Richter [h], G. Schrieder [h], A. Zilges [i], M.O. Distler [j], H. Merkel [j], U. Müller [j], A.R. Junghans [k], H. Lenske [l], M. Fujiwara [m], T. Suda [n], S. Kato [o], T. Adachi [p], S. Hamieh [p], M.N. Harakeh [g,p], N. Kalantar-Nayestanaki [p], H. Wörtche [p], G.P.A. Berg [p,q], I.A. Koop [r], P.V. Logatchov [r], A.V. Otboev [r], V.V. Parkhomchuk [r], D.N. Shatilov [r], P.Y. Shatunov [r], Y.M. Shatunov [r], S.V. Shiyankov [r], D.I. Shvartz [r], A.N. Skrinsky [r], L.V. Chulkov [s], B.V. Danilin [s,1], A.A. Korsheninnikov [s], E.A. Kuzmin [s], A.A. Ogloblin [s], V.A. Volkov [s], Y. Grishkin [t], V.P. Lisin [t], A.N. Mushkarenkov [t], V. Nedorezov [t], A.L. Polonski [t], N.V. Rudnev [t], A.A. Turinge [t], A. Artukh [u], V. Avdeichikov [u,ac], S.N. Ershov [u], A. Fomichev [u], M. Golovkov [u], A.V. Gorshkov [u], L. Grigorenko [u], S. Klygin [u], S. Krupko [u], I.N. Meshkov [u], A. Rodin [u], Y. Sereda [u], I. Seleznev [u], S. Sidorchuk [u], E. Syresin [u], S. Stepantsov [u], G. Ter-Akopian [u], Y. Teterev [u], A.N. Vorontsov [u], S.P. Kamerdzhiev [v], E.V. Litvinova [v,g], S. Karataglidis [w], R. Alvarez Rodriguez [y], M.J.G. Borge [x], C. Fernandez Ramirez [y], E. Garrido [x], P. Sarriguren [x], J.R. Vignote [x], L.M. Fraile Prieto [y], J. Lopez Herraiz [y], E. Moya de Guerra [y], J. Udias-Moinelo [y], J.E. Amaro Soriano [z], A.M. Lallena Rojo [z], J.A. Caballero [aa], H.T. Johansson [ab], B. Jonson [ab], T. Nilsson [ab], G. Nyman [ab], M. Zhukov [ab], P. Golubev [ac], D. Rudolph [ac], K. Hencken [ad], J. Jourdan [ad], B. Krusche [ad], T. Rauscher [ad], D. Kiselev [ad,al], D. Trautmann [ad], J. Al-Khalili [ae], W. Catford [ae], R. Johnson [ae], P.D. Stevenson [ae], C. Barton [af], D. Jenkins [af], R. Lemmon [ag], M. Chartier [ah], D. Cullen [ai], C.A. Bertulani [aj], A. Heinz [ab,ak]

[a] INRNE-BAS Sofia, Bulgaria
[b] Centre d'Etudes Nucléaires Bordeaux-Gradingnan (CENBG), France
[c] CEA Bruyères-le-Châtel, France
[d] CEA Saclay, France
[e] GANIL Caen, France
[f] IPN Orsay, France
[g] GSI Darmstadt, Germany
[h] TU Darmstadt, Germany
[i] University of Cologne, Germany
[j] Johannes Gutenberg University of Mainz, Germany
[k] FZ Dresden, Germany
[l] Justus-Liebig University Giessen, Germany
[m] RCNGP Osaka, Japan
[n] RIKEN, Japan
[o] Yamagata University, Japan
[p] KVI, University of Groningen, The Netherlands
[q] Department of Physics and JINA, University of Notre Dame, USA
[r] BINP Novosibirsk, Russia
[s] NRC Kurchatov Institute Moscow, Russia
[t] INR Moscow, Russia
[u] JINR Dubna, Russia
[v] IPPE Obninsk, Russia
[w] University of Johannesburg, Department of Physics, South Africa
[x] Instituto de Estructura de la Materia, CSIC Madrid, Spain
[y] Grupo de Physica Nuclear, Complutense University of Madrid, Spain
[z] Departamento de FAMN, Granada University, Spain

0168-9002/$ - see front matter © 2011 Elsevier B.V. All rights reserved.
doi:10.1016/j.nima.2010.12.246

[aa] Departamento de FAMN, Seville University, Spain
[ab] Chalmers University of Technology, Sweden
[ac] Lund University, Sweden
[ad] University of Basel, Switzerland
[ae] University of Surrey, United Kingdom
[af] University of York, United Kingdom
[ag] CCLRC Daresbury, United Kingdom
[ah] University of Liverpool, United Kingdom
[ai] University of Manchester, United Kingdom
[aj] Texas A&M University Commerce, USA
[ak] Yale University, USA
[al] Paul Scherrer Institute, Switzerland

ARTICLE INFO

Article history:
Received 20 October 2009
Received in revised form
21 December 2010
Accepted 21 December 2010
Available online 11 February 2011

Keywords:
eA collider
Electron scattering
Nuclei far off stability

ABSTRACT

The electron–ion scattering experiment ELISe is part of the installations envisaged at the new experimental storage ring at the International Facility for Antiproton and Ion Research (FAIR) in Darmstadt, Germany. It offers an unique opportunity to use electrons as probe in investigations of the structure of exotic nuclei. The conceptual design and the scientific challenges of ELISe are presented.

© 2011 Elsevier B.V. All rights reserved.

1. Introduction

The Facility for Antiproton and Ion Research (FAIR) is scientifically and technically one of the most ambitious projects worldwide. It has a broad scientific scope allowing forefront research in different sub-disciplines of physics. Because of its great potential for discoveries, the FAIR project has been given highest priority in the NuPECC Long-Range Plan 2004 [1]. One of the scientific pillars of FAIR is nuclear-structure physics and nuclear astrophysics with radioactive ion beams. The proposed electron–ion collider (eA Collider) consisting of the New Experimental Storage Ring (NESR) and the Electron and Antiproton Ring (EAR) will allow a range of novel studies with stored and cooled beams.

The use of electrons as probe provides a powerful tool for examining nuclear structure. The most reliable picture of nuclei originates in electron scattering. The increasing number of publications devoted to theoretical treatments of electron scattering off exotic nuclei [2–14] supports this assertion and underlines the usefulness of an electron–ion scattering setup for unstable nuclei. However, up to now, this technique is still restricted to stable isotopes. The Electron–Ion Scattering experiment (ELISe) aims at an extension of this powerful method to radioactive nuclei outside the valley of stability. ELISe will be a unique and unprecedented tool for precise measurements of nuclear–charge distributions, transition charge and current matrix elements, and spectroscopic factors. This capability will contribute to a variety of high-quality nuclear-structure data that will become available at FAIR.

A first technical proposal for an electron–ion collider was made almost 20 years ago at the Joint Institute for Nuclear Research (Dubna) [15]. The ideas of this proposal have been incorporated in and further developed at the RIKEN Rare-Isotope Beam Factory (RIBF) for the so-called Multi-USe Experimental Storage (MUSES) rings [16], as well as at the planned eA collider at FAIR, under the name ELISe [17–21]. However, none of these projects has been realized up to now. For the RIBF, an alternative setup called SCRIT (Self-Contained Radioactive Ion Target) has been proposed [22]. In SCRIT a circulating beam of electrons scatters off ions stored in a trap. Within foreseeable future, ELISe could be the first and only eA collider for radioactive ion beams worldwide. The ELISe setup provides easy access to different types of electron–nucleus reactions in experiments where scattered electrons are detected in coincidence with reaction products.

A cooled beam consisting of radioactive ions stored in the NESR will be brought to collision with an intense electron beam circulating in EAR at the interaction point (IP). Here, a magnetic spectrometer for the detection of scattered electrons as well as detector systems for the measurements of reaction products are to be installed.

This paper is organized as follows. It describes the physics case for ELISe and explains the conditions and requirements for performing different experiments. We explain the difference between fixed target and colliding beam kinematics and outline the planned design and predicted performance of the eA collider. The major components of ELISe, being planned as multi-purpose setup for these experiments, i.e. an electron and in-ring spectrometer, as well as a luminosity monitor, are characterized and viable concepts for their design are presented.

2. Research objectives

The central goal in nuclear physics is the construction of a theoretical framework capable of describing consistently all nuclear systems from the deuteron two-body case to infinite nuclear matter, going through every finite nucleus with its many degrees of freedom and modes of excitation and decay. This ambition is also the driving force for experimental investigations of nuclei near the limits of stability. In the past two decades, substantial progress towards this goal has been made due to the progress in developments of radioactive beams. Intensive studies of the structure of nuclei near the drip lines are carried out at several laboratories as GSI in Darmstadt (Germany), GANIL in Caen (France), ISOLDE at CERN (Switzerland), JINR in Dubna (Russia), NSCL at Michigan State University (USA) and RIKEN (Japan). The studies involve nucleus–nucleus or nucleon–nucleus interactions as well as decay studies and different means to determine their ground state properties. Building on the great progress in the experimental and theoretical investigations

* Corresponding author. Tel.: +49 6159 71 2887; fax: +49 6159 71 2809.
E-mail address: H.Simon@gsi.de (H. Simon).

[1] Deceased.

(see, for example, the reviews [23,24]), novel experimental methods and observables will most certainly enhance the opportunities leading to a better understanding of the structure of nuclei near the limits of stability and in general.

Electron scattering, as in ELISe, offers unique and widely recognized advantages for the study of nuclear structure (see reviews [25–29]). Interactions with electrons are well described by the most accurate theory in physics—quantum electrodynamics (QED). The coupling is weak, so that multiple scattering effects are strongly suppressed, such that perturbations of the initial state of the nucleus are minimal. The ability to vary momentum and energy transferred to the nucleus, independently, allows mappings of spatial distributions of the constituent particles. Since electrons are point particles, they offer excellent spatial resolution, and can additionally be tuned to the scale of a process under study. Electron scattering, as it will be performed at ELISe, will thus add important new observables to investigate radioactive nuclear species.

To mention selected physics aspects (see also Table 1), these experiments will give access to

- charge–density distributions, in particular root-mean-square (r.m.s.) radii, of exotic nuclei from elastic electron scattering,
- new specific collective modes of excitation with selectivity to multipolarities via inelastic electron scattering, and
- internal nucleon–nucleon correlations and nuclear structure from quasi-free scattering, such as nucleon (e,e′N) or cluster (e,e′c) knockout.

2.1. Elastic electron scattering: charge density distributions, charge radii

Neglecting Coulomb distortion, i.e. in first order Born approximation (BA), the cross-section for the scattering of an electron off a nucleus is given by

$$d\sigma/d\Omega = d\sigma/d\Omega_{\mathrm{Mott}} F^2(q). \quad (1)$$

Here $d\sigma/d\Omega_{\mathrm{Mott}}$ is the cross-section in BA for the scattering off a point nucleus with spin zero and $F(q)$ is the form factor, which contains the information about the nuclear charge distribution $\rho(r)$. To be specific: The form factor is the Fourier transform of the latter.

Table 1
Required luminosities for different studies. The achievable values predicted for the ELISe setup will be discussed in Section 4. The given values are based on rate estimates for—at most—4 week measurements.

Reaction	Deduced quantity	Target nuclei	Luminosity ($\mathrm{cm^{-2}s^{-1}}$)
Elastic scattering at small q	r.m.s. charge radii	Light	10^{24}
		Medium	
First minimum in elastic form-factor	Density distribution with 2 parameters	Light	10^{28}
		Medium	10^{26}
		Heavy	10^{24}
Second minimum in elastic form-factor	Density distribution with 3 parameters	Medium	10^{29}
		Heavy	10^{26}
Giant resonances	Position, width, strength, decays	Medium	10^{28}
		Heavy	10^{28}
Quasi-elastic scattering	Spectroscopic factors, spectral function, momentum distributions	Light	10^{29}

Since BA is not sufficiently precise for the scattering off nuclei with larger Z, the cross-section has to be calculated by solving the Dirac equation numerically with the Coulomb potential from $\rho(r)$, for which an ansatz has to be made for this purpose. The common method is the calculation of the phase shifts of the electron wave in the Coulomb potential of $\rho(r)$ [30], it is therefore called "phase shift" or, thinking of the distorted electron waves, "DW" method.

The charge distribution is determined from measured cross-sections by fitting the free parameters of the ansatz for $\rho(r)$ to the data. Several aspects of the information gained by such experiment are easier to catch by looking at the form factor (some details of how one gets it will be discussed in Section 4.2).

The existing information on charge densities obtained from electron scattering experiments for more than 300 nuclides is reviewed in Refs. [31,32]. These data, confined to the valley of stability, show oscillations in r.m.s. radii, surface thicknesses, and interior densities as a function of atomic number [33,34]. The r.m.s. charge radius, can be extracted in a model-independent way from experimental data at low q from the expansion

$$F_{\mathrm{ch}}(q) \sim 1 - \frac{\langle r^2 \rangle}{3!} q^2 + \frac{\langle r^4 \rangle}{5!} q^4 + \cdots. \quad (2)$$

The surface thickness, defined as the distance where $\rho_{\mathrm{ch}}(r)$ drops from 90% to 10% of its central value, is also accessible from the extracted form factor. For unstable nuclei, no data on the shapes of the nuclear surfaces exist, and here ELISe could provide a first insight. A central-density depression was observed in several nuclei [35], even including light nuclei [36]. Such a depression is predicted for proton-rich [12,14] and superheavy [37–39] nuclei. The origin of this is due to Coulomb effect, the underlying shell and single particle structure as well as short-range correlations (see for example Ref. [35,40] and references therein). The systematics of the charge–density distributions with the inclusion of nuclei having extreme proton–neutron asymmetry forms a basis for investigations addressing both the structure of nuclei and the properties of bulk nuclear matter. An example of the latter is the determination of nuclear compressibility from experimental nuclear radii and binding energies [41].

The most realistic description of elastic electron-scattering cross-sections can be achieved by solving the Dirac equation, and performing an exact phase-shift analysis [30]. This method has been chosen, e.g. in Ref. [7]. Using the DW method, the modulus of the charge form factor can be determined from the differential cross-section. Its sensitivity to changes in the charge distribution is demonstrated in Fig. 1, taken from Ref. [7], where Ni isotopes are shown as example. The proton densities presented in Fig. 1 were obtained from self-consistent HF+BCS mean-field calculations with effective *NN* interactions in a large harmonic-oscillator basis [42] by using a density-dependent Skyrme parameterization. In the same figure, the squared moduli of charge form factors, which are obtained from solving the Dirac equation numerically, are presented. Following this prescription, electron scattering is computed in the presence of a Coulomb potential induced by the charge distribution of a given nucleus. The intrinsic charge distribution of the neutron is included into these calculations. Two codes were used for the numerical evaluation of the form factors: the first is taken from Ref. [43] which follows Ref. [30] and the second has been discussed in Ref. [44]. The results of both calculations were found to be in good agreement. The nuclear charge form factor $F_{ch}(q)$ has been calculated as follows:

$$F_{ch}(q) = \left[F_{point,p}(q) G_{Ep}(q) + \frac{N}{Z} F_{point,n}(q) G_{En}(q) \right] F_{c.m.}(q) \quad (3)$$

where $F_{point,p}(q)$ and $F_{point,n}(q)$ denote the form factors related to the point-like proton and neutron densities $\rho_{point,p}(\mathbf{r})$ and

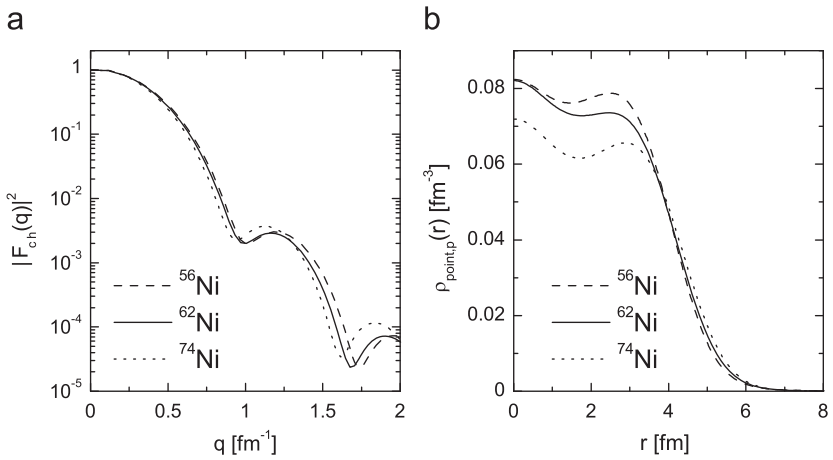

Fig. 1. Modulus squared of charge form factors (panel (a)) calculated by solving the Dirac equation with HF+BCS proton densities (panel (b)) for the unstable doubly magic ^{56}Ni, stable ^{62}Ni and unstable ^{74}Ni isotopes [7]. In the calculation of the moduli, the intrinsic charge distribution of the neutron was taken into account; see text for more details.

$\rho_{point,n}(\mathbf{r})$, respectively [7]. These densities correspond to wave functions where the positions $\mathbf{r}$ of the nucleons are defined with respect to the center of the potential in the laboratory system. In order to let $F_{ch}(q)$ correspond to the density distributions in the center-of-mass coordinate system, a factor $F_{c.m.}(q)$ is introduced (e.g. Refs. [45–47]) in two commonly used ways:

$$F_{c.m.}(q) = e^{(qR)^2/6A} \tag{4}$$

where R stands for the root-mean-square radius of the nucleus, or

$$F_{c.m.}(q) = e^{(qb)^2/4A} \tag{5}$$

where b denotes the harmonic-oscillator parameter. For shell model potentials different from harmonic-oscillator, Eqs. (4) and (5) are approximations.

Eq. (3) with a c.m. correction of form (4) [47] was used to compute the modulus squared of the form factor that can be extracted also from experimental data. In Eq. (3) $G_{Ep}(q)$ and $G_{En}(q)$ denote Sachs proton and neutron electric form factors, respectively, and are taken from one of the most recent phenomenological parameterizations [48]. Actually, there is no significant difference between this recent parameterization and the most traditional one of Refs. [49–51] for the momentum transfer range considered in this work ($q < 4$ fm^{-1}).

In general, it has been found that with increasing number of neutrons in a given isotopic chain the minima of the curves of the charge form factor are shifted towards smaller values of the momentum transfer [7]. This is due mainly to the enhancement of the proton densities in the peripheral region and to a minor extent to the contribution from the charge distribution of the neutrons themselves. By accounting for the Coulomb distortion of the electron waves, a filling of the Born zeros is observed when the DW method is used (in contrast to plane-wave Born approximation).

As evident from Eq. (2), the r.m.s. radius is accessible from measurements at very low q-values where the cross-sections are large. An accurate determination of the charge distributions to e.g. extract the surface thickness from measured differential cross-sections, requires a high precision measurement in a wide region of transferred momentum, at least up to the second maximum. As a further example, we quote the formation of so-called bubbles in exotic nuclei as discussed in Ref. [12], where the depletion of the central part of the charge distribution is attributed to a depopulation of s-states. It is also argued that cross-section measurements to the second form-factor minimum, already provide information on the depletion of the central density. The data obtainable with ELISe can provide for the first time precise information on the charge distribution of radioactive nuclei through form-factor measurements. These data could subsequently be used to benchmark theoretical models for the structure of exotic nuclei.

2.2. Inelastic scattering: giant resonances, decay channels, astrophysical applications

Inelastic electron scattering has proven to be a powerful tool for studying properties of excited states of nuclei, in particular their spins, parities, and the strength and structure of the transition densities connecting the ground and excited states (see e.g. Ref. [25]). Although important information is available from other types of experiments, as for example, hadron scattering, pickup and transfer reactions, charge–exchange reactions, the electron-scattering method has unique features. This is the only method which can be used to determine the detailed spatial distributions of the charge transition densities for a variety of single-particle and collective transitions. These investigations provide a stringent test of the nuclear many-body wave functions [26,27].

Due to its strong selectivity, collective and strong single-particle excitations can be studied particularly well in electron scattering. Electric and magnetic giant multipole resonances are of special interest, and several of them have been discovered and studied using electron scattering (see Ref. [28] and references therein).

When approaching the neutron drip-line, there is a characteristic increase in the difference between neutron and proton density distributions. Apart from direct measurements using elastic scattering as described in the last section, where electron and hadron scattering results are combined to extract the neutron-skin density distribution, also complementary indirect methods are available. The difference in radii of the neutron and proton density distributions is accessible via studies of giant dipole resonances (GDR) by inelastic scattering of an isoscalar probe or spin-dipole resonances by charge–exchange reactions. The cross-section of these processes strongly depends on the relative neutron-skin thickness [52,53]. This quantity is of great importance due to direct relations between the neutron-skin thickness and properties of the nuclear matter EOS such as the symmetry-energy coefficient and the nuclear incompressibility. The energy of the isoscalar giant monopole-resonance can be used to deduce the compressibility of nuclear matter, which is directly related to

the curvature of the EOS. Hence data from inelastic electron scattering can provide an independent test of this quantity in addition to those obtained from the nuclear radius (elastic scattering) and the binding energy (see Ref. [41]). Magnetic dipole excitations (M1) arise due to changes in the spin structure of the nucleus and orbital angular motion of its constituents. Along with decay studies, the measured M1 distributions from electron scattering could provide information about the nuclear Gamow–Teller strength distribution. The latter is important for reliably extracting inelastic neutrino–nucleus cross-sections [54], which are important in certain astrophysical scenarios, such as neutron stars or core-collapse supernovae.

The low-energy dipole strength located close to the particle-emission threshold is a general feature in many isospin-asymmetric nuclei [55]. This mode is known as the Pygmy Dipole Resonance (PDR), and has been explained as being generated by oscillations of weakly bound neutrons with respect to the isospin symmetric core in neutron-rich nuclei (see review [56]). Thus, in exotic nuclei the PDR modes should be especially pronounced.

The origin of approximately one half of the nuclides heavier than iron observed in nature is explained by the r-process. The existence of pygmy resonances has important implications on theoretical predictions of radiative neutron-capture rates in the r-process nucleosynthesis, and consequently on the calculated elemental abundance distribution in the universe. This was studied using calculations and fits to the properties of neutron-rich nuclei involved in this process [57]. The inclusion of the PDR increases the r-process abundance-distributions for nuclei around $A=130$ by about two orders of magnitude (Fig. 6 in Ref. [57]) as compared with the case where only the GDR was taken into account. The result of the calculations strongly depends on the competition between the open decay channels.

In heavy nuclei, the r-process path is expected to be limited by fission, and the fission process is treated only very schematically in network calculations. Therefore electro-induced fission giving access to a multipole decomposition of the fission cross-sections will allow to refine models of the fission process, to study the nuclear structure involved, and to serve as an improved input for r-process calculations [58] since fission is one of the decay channels of the excited nucleus. ELISe will be an ideal experiment for electro-fission studies. Measurements of coincidences between the scattered electron and the nuclear decay products represent the most powerful tool available for precise determinations of multipole excitation functions even when the resonance strength is spread over a wide excitation energy range [59]. The proton and neutron numbers of fission fragments and their kinetic energies as a function of the excitation energy can be determined. Such complete experimental information will enable, for the first time, studies of the influences of neutron and proton shells as well as of pairing correlations on fission dynamics. Also, fission barriers of exotic nuclei can be determined precisely.

2.3. Quasi-free scattering (QFS): shell structure, spectral functions, spectroscopic factors

High-resolution exclusive (e,e′p) experiments offer the possibility to study individual proton orbits [60–62]. In Ref. [61] the momentum distribution for "single"-particle states were thus determined. These were fitted by combinations of bound-state wave-functions generated in a Woods–Saxon potential. Thereby, the r.m.s. charge radii and the depletion of the spectroscopic factors could be determined. This can be used to observe knock-out from regions inside the nucleus with essentially different densities. The observed spectroscopic strength for valence shells, obtained with (e,e′p) reactions, are surprisingly small, sometimes by 30–50%, compared to values of shell model calculations. It is believed that this is due to effects of short-range correlations [63,64]. For asymmetric nuclei neutron–proton interactions lead to a reordering of shells [65]. It is therefore important also to characterize deeper lying levels. Measured momentum distributions will help to identify the angular momentum and quantum numbers of the involved shells. Effects of final-state interactions and meson-exchange currents can be substantially reduced by choosing parallel kinematics [67,68]. The quasi-free (e,e′p) scattering-condition $Q^2/2m\omega_0 \approx 1$ in the eA collider[2]—where Q denotes the four momentum transfer and ω_0 the energy loss—can be realized already at moderately forward scattering angles between 50° and 60°. Exclusive measurements should therefore be possible for light elements, where the achievable luminosities are close to $10^{29}\,\mathrm{cm}^{-2}\,\mathrm{s}^{-1}$, as will be shown later in this paper. Occupation probabilities and spectroscopic factors can be obtained in the region of resolved states. Another access to correlations in the nuclear interior isprovided by cluster knock out (e,e′c) [3] that yields information on momentum distributions and cluster spectroscopic factors of clusters inside nuclei.

In inclusive electron scattering in the quasi-free region, an average over all available orbits can be measured [66] by the shape of the obtained spectrum. Inclusive measurements are likely to be feasible for medium and heavy nuclei at achievable luminosities of $10^{28}\,\mathrm{cm}^{-2}\,\mathrm{s}^{-1}$.

3. Kinematics of colliding beams

This section describes the kinematics of colliding beams and the design parameters of the electron spectrometer. It is compared to a conventional laboratory system where the electron beam strikes a fixed target. The scattering process is described in a polar coordinate system with the axis along the electron beam axis where the polar angle is the scattering angle θ. In the following, this system is referred to as kinematics F. The boosted center-of-mass (c.m.) of the colliding beams into the laboratory frame leads to kinematical conditions that are very different compared to conventional experiments.

The equations in this section are calculated in the limit of zero electron mass. In this limit the total energy of the electron is equal to its kinetic energy and momentum ($E_e = T_e = p_e$).[3] The numerical estimates given in this section assume counter-propagating, i.e. colliding beams of 0.74 GeV/nucleon ions and 0.5 GeV electrons (referred to as kinematics C). The energy of electrons in kinematics F corresponding to that of colliding beam kinematics in the c.m. is given by

$$T_e(F) = \sqrt{\frac{1+\beta}{1-\beta}}\,T_e(C) \tag{6}$$

where $\beta = p_A/E_A$ is the ion velocity. Thus, a 0.5 GeV electron in kinematics C corresponds to a 1.64 GeV electron in kinematics F.

Table 2 gives the kinematical equations for two types of kinematics for an electron scattering experiment. It can be shown that while the energy of elastically scattered electrons in kinematics F is almost independent of the scattering angle, the electron energy in kinematics C depends strongly on scattering angle and increases from $p_{e'} = p_e$ to $p_{e'} \approx (1+\beta)/(1-\beta)p_e$ when the

[2] For the simulation calculation (QFS on ^{12}C), going beyond the scope of this work, ω_0 was taken to be 135 MeV. Protons are then emitted in backward direction in a small cone with angles ranging from 160° to 165°. The required proton resolution for resolving states varies from about 1% to 3% at 300 and 800 MeV, respectively. The $A-1$-fragments fall within the acceptance of the in-ring spectrometer, described later in this paper.

[3] Natural units $c=1$, $\hbar=1$ are used in the following.

Table 2
Kinematics of colliding beams. Here, p_e, $p_{e'}$ are the momenta of incoming and scattered electrons, θ is the electron scattering angle relative to the electron beam direction, $\beta = p_A/E_A$, $\delta = \sqrt{(1-\beta)/(1+\beta)}$, $E_A = \sqrt{M^2+p_A^2}$ is the total energy of incident ions, and E^* the excitation energy of the recoil ion.

F	C
Conventional kinematics ($\beta = 0$)	Counter-propagating beams ($\beta > 0$)
Scattered electron momentum	
$p_{e'} = \dfrac{p_e - E^*}{1 + 2\frac{p_e}{M}\sin^2\frac{\theta}{2}}$	$p_{e'} = \dfrac{p_e - \delta E^*}{1 + 2\frac{p_e - p_A}{M}\delta\sin^2\frac{\theta}{2}}$
Momentum transfer	
$q^2 = \dfrac{4p_e^2\sin^2\frac{\theta}{2}}{1 + 2\frac{p_e}{M}\sin^2\frac{\theta}{2}}$	$q^2 = \dfrac{4p_e^2\sin^2\frac{\theta}{2}}{1 + 2\delta\frac{p_e - p_A}{M}\sin^2\frac{\theta}{2}}$
Resolution (momentum dependence)	
$\Delta E^* \approx -\left(1 + 2\frac{p_e}{M}\sin^2\frac{\theta}{2}\right)\Delta p_{e'}$	$\Delta E^* \approx -\left(\frac{1}{\delta} + 2\frac{p_e - p_A}{M}\sin^2\frac{\theta}{2}\right)\Delta p_{e'}$
Resolution (angular dependence)	
$\Delta E^* \approx -\dfrac{p_e p_{e'}}{M}\sin\theta\Delta\theta$	$\Delta E^* \approx -\dfrac{(p_e - p_A)p_{e'}}{M}\sin\theta\Delta\theta$

angle increases from 0° to 180°, i.e. from 0.5 GeV at zero degree to ≈5 GeV in backward direction. Furthermore, while in kinematics F the energy separation between elastically and inelastically scattered electrons is approximately equal to the excitation energy (E^*) of the recoiling ion, in kinematics C this separation is reduced by a factor of $\sqrt{(1-\beta)/(1+\beta)} \approx 0.3$.

These two features of kinematics C make it difficult to resolve elastically and inelastically scattered electrons.[4]

The strong variation of the scattered electron energy with angle results in an extreme sensitivity to the uncertainty in the polar angle determination. It is shown in Table 3, to be a factor of 40 larger for a ^{50}Co beam colliding with 0.5 GeV electrons than in a fixed-target kinematics with equivalent electron energy (1.64 GeV). This factor increases to about 400 for beams of ^{132}Sn. The sensitivity to the uncertainty in absolute value of the scattered electron momentum is about the same in both systems.

The colliding beam kinematics, however, allows identifying the residual nucleus in coincidence with the scattered electron. Reaction products, including nucleons and γ-rays, can be detected using specific sub-detector systems. In addition, the detector setup allows to identify A and Z for the fragments, as shown in Section 6. Their momenta and energies can be determined and the reaction kinematics can be reconstructed. This, in turn, allows a unique classification of the observed reaction. In addition, the use of the coincidence method results in a strong reduction of the unavoidable radiative background seen in conventional inclusive electron-scattering experiments.

4. Conceptual design of the electron–nucleus collider at NESR

The conceptual layout of the collider facility is presented in Fig. 2. It consists of two rings with different circumferences: the electron ring EAR with electron energies between 0.2 and 0.5 GeV, and the ion ring NESR, which will operate at a set of discrete energies between 0.2 GeV/nucleon up to 0.74 GeV/nucleon. The electron ring is filled with electrons from a pulsed linac. NESR is supplied with pre-cooled fragment beams from a dedicated Collector Ring (CR) which is capable of cooling the secondary beams stochastically to primary beam quality within approximately 1.5 s.

The electron ring is placed outside the main ion ring, so that a bypass beam line connects NESR with EAR and provides sufficient space for the electron spectrometer and a recoil detector system. The ion and electron beam trajectories intersect at an interaction point (IP) around which the electron spectrometer as well as auxiliary detectors for measuring the reaction products are placed. The IP is also viewed along the straight section through bore holes in the dipole magnets, that allow for installing the luminosity monitor described in Section 7.

4.1. General considerations

The main parameters for the two rings and a hypothetical neutron-rich uranium isotope, with $A/Z = 2.7$ and kinetic energy 0.74 GeV/nucleon (this energy corresponds to a velocity $\beta_A = 0.8303$ and a rigidity of 12.5 Tm), are listed in Table 4. The ratio between the revolution frequencies of electrons and ions n should be an integer. Beam-beam effects require that n is as small as possible. An acceptable value for the highest ion energy 0.74 GeV/nucleon is $n = 5$. Then a discrete set of other possible energies is: 0.3587 GeV/nucleon ($n = 6$), 0.2254 GeV/nucleon ($n = 7$). If the circumference of the NESR orbit is taken to be 222.916 m, then 53.693 m are required for the circumference of the EAR. For the proposed beam-optics both beams are flat at IP, with horizontal beam sizes of $\sigma_x = 210$ μm and 220 μm and vertical beam sizes of $\sigma_y = 85$ μm and 87 μm for the EAR and NESR, respectively.

The momentum spread of the electron beam at the interaction zone restricts the achievable resolution for the transferred energy and momentum in electron scattering experiments considerably. The momentum spread of the beam is shown in Fig. 3 as function of the electron energy. It depends mainly on two effects: (i) intra-beam scattering (IBS) and (ii) statistical fluctuations due to synchrotron radiation. IBS is an effect where collisions between particles bring charged particles closer to thermal equilibrium in a bunch and generally causes the beam size and the beam-energy spread to grow. This effect limits as well luminosity and lifetime. IBS gives a relationship between the size of the beam and the number of particles it contains, and leads therefore to a limit for the maximally achievable luminosity [69]. The emission of quanta in synchrotron radiation is a Poisson process. This process leads to a decrease of the mean energy of electrons due to radiation losses [70] and to an increase of the energy spread in a bunch caused by statistical fluctuations.

Assuming transverse Gaussian distributions for the bunches, the luminosity (L) in a collider is given by

$$L = F_e n_e \frac{N_e N_A}{4\pi\sigma_x\sigma_y}. \quad (7)$$

Thus, options for a substantial increase of luminosity include the reduction of beam sizes at the interaction zone $\sigma_{x,y}$ and/or an increase of bunch population (N_e, N_A), number of colliding bunches n_e (or n_A) and revolution frequencies F_e (or F_A). However, the decrease of $\sigma_{x,y}$ or an increase of N_e, N_A unavoidably also increases the intra-beam scattering, and beam–beam forces which lead to collective (coherent) and incoherent beam–beam instabilities and thus to a reduction of the luminosity. In the case of a very intense ion beam, the space–charge effect results in an upper limit of the luminosity $L_{\mathrm{sp.ch.}}$, which does not depend on the

[4] Table 2 demonstrates that the separation between elastic and inelastic peaks in the spectrum is much larger in the case of co-propagating beams. However, several other parameters are not in favor of this geometry. For example, the length $\mathcal{L}$ of interaction zone (IZ) is determined by $\mathcal{L} \approx l/(1 \pm \beta)$, where l is the ion-bunch length, + corresponds to counter-propagating beams and − to co-propagating beams. For co-propagating beams $\mathcal{L} = 50$ cm, which is 10 times larger than for counter-propagating beams.

Table 3
Comparison of colliding beam and conventional fixed-target kinematics. Calculations were performed assuming counter-propagating beams of 0.74 GeV/nucleon ^{50}Co and 0.5 GeV electrons. In fixed-target kinematics this is equivalent to a 1.642 GeV electron beam. Here, θ and $p_{e'}$ are the scattering angle and the scattered-electron momentum. The quantities $(\partial E^*/\partial\theta)\Delta\theta$ and $(\partial E^*/\partial p)\Delta p$ show the sensitivity of the excitation energy determination to the uncertainties in the scattering angle and in the scattered-electron momentum ($\Delta\theta = 1$ mrad and $\Delta p/p = 10^{-4}$).

q (GeV/c)	Kinematics C				Kinematics F			
	θ (deg)	$p_{e'}$ (GeV/c)	$\frac{\partial E^*}{\partial\theta}\Delta\theta$ (MeV)	$\frac{\partial E^*}{\partial p}\Delta p$ (MeV)	θ (deg)	$p_{e'}$ (GeV/c)	$\frac{\partial E^*}{\partial\theta}\Delta\theta$ (MeV)	$\frac{\partial E^*}{\partial p}\Delta p$ (MeV)
0.1	11.4	0.504	0.15	−0.16	3.5	1.642	−0.004	−0.16
0.2	22.7	0.518	0.30	−0.16	7.0	1.642	−0.007	−0.16
0.3	33.5	0.540	0.44	−0.16	10.5	1.642	−0.010	−0.16
0.4	43.9	0.572	0.59	−0.16	14.0	1.642	−0.014	−0.16
0.5	53.7	0.613	0.73	−0.16	17.5	1.642	−0.017	−0.16
0.6	62.8	0.662	0.87	−0.16	21.1	1.642	−0.021	−0.16

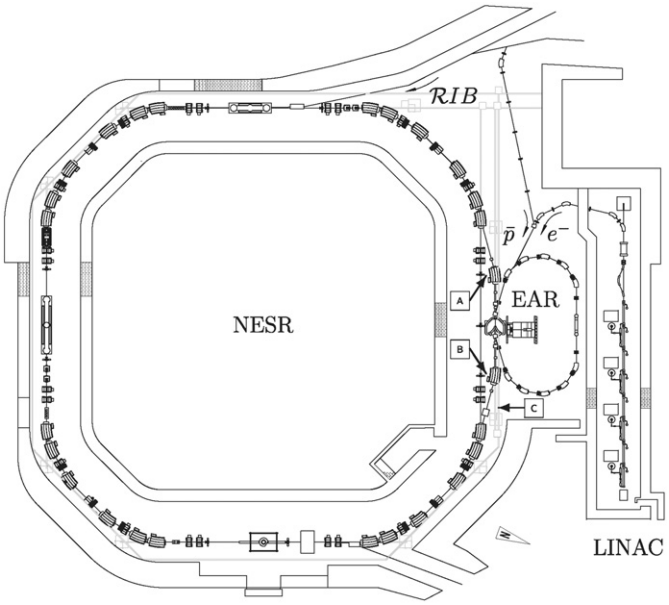

Fig. 2. Schematic layout of the New Experimental Storage Ring (NESR, circumference 222.9 m) for Rare Isotope Beams (RIB) and the Electron Antiproton Ring (EAR, circumference 53.7 m). Electrons with energies ranging from 125 to 500 MeV will be provided by an electron linac and stored in the EAR. Antiprotons can be directed from a dedicated collector ring (not shown) into the EAR via a separate beam line. The intersection between EAR and NESR is equipped with an electron spectrometer setup which will be discussed in the following. The free space opposing the spectrometer can be equipped with experiment specific detectors. The arrow at C points to the place where an optical bench is situated, from which the intersection can be viewed through a 10 cm hole in the dipole magnet. A luminosity monitor, based on bremsstrahlung detection, discussed in Section 7, and LASER installations for atomic physics experiments can be installed here. For a detailed discussion of the bypass section (A–B) see text.

number of ions in the bunches, is given by

$$L_{\mathrm{sp.ch.}} = F_e n_e \frac{A}{Z^2}\frac{N_e \Delta\nu\gamma^3\beta^2}{4\pi r_p\sqrt{\beta_x\beta_y}}\frac{2\sqrt{2\pi}\sigma_s}{R} \tag{8}$$

where r_p is the classical proton radius, β and γ are the Lorentz factors. For the other variables, see definitions in Table 4.

Apart from the above-mentioned limitations leading to a flat plateau of maximally achievable luminosities, as can be seen in Fig. 4, the production and preparation of secondary beams strongly influence the total number of unstable isotopes available for experimental studies at the outer part of the nuclear landscape. Table 5 shows a selection of the numerical results as depicted also in Fig. 4.

Table 4
General parameters of the electron–nucleus collider assuming a 0.74 GeV/nucleon uranium beam.

	Units	EAR	NESR
Circumference	m	53.693	222.916
Bending radius, r	m	1.75	8.125
Maximum energy	GeV, GeV/nucleon	0.5	0.74
Revolution frequency, F_e, F_A	MHz	5.585	1.117
Number of bunches, n_e, n_A		8	40
Bunch population, N_e, N_A	particles	5×10^{10}	0.86×10^{7}
Bunch length, σ_s	cm	4	15
Beam size at IP, $\sigma_{x,y}$	μm	210; 85	220; 87
Momentum spread, $\Delta p/p$	%	3.6×10^{-2}	4×10^{-2}
Beam divergence at IP, $\sigma_{x0,y0}$	mrad	0.22; 0.58	0.22; 0.58
Beta function at IP, $\beta_{x,y}$	cm	100; 15	100; 15
Laslett tune shift, $\Delta\nu$			0.08
Luminosity	$\mathrm{cm^{-2}\,s^{-1}}$	10^{28}	

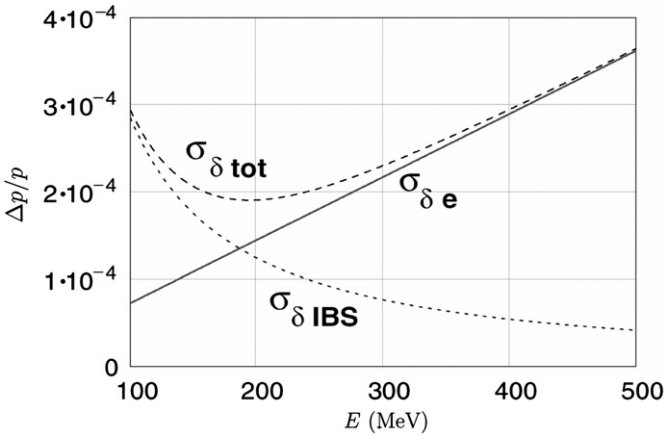

Fig. 3. Dependence of the electron-beam momentum spread $\Delta p/p$ on the electron-beam energy E. Here $\sigma_{\delta e}$ denotes the contribution to the momentum spread from statistical fluctuations due to synchrotron radiation, $\sigma_{\delta IBS}$ is caused by intra-beam scattering, and $\sigma_{\delta tot}$ denotes the total momentum spread.

(i) We start with an optimized production scheme, taking the maximum for the yield [71] and including the acceptance of the Super FRagment Separator (Super-FRS) [72] for fission and fragmentation reactions, whilst the available primary beams are varied. The mass-resolution [73] in the separator depends on the choice of the niobium degraders that are used in order to distinguish differently charged ions using the $B\rho-\Delta E-B\rho$ method

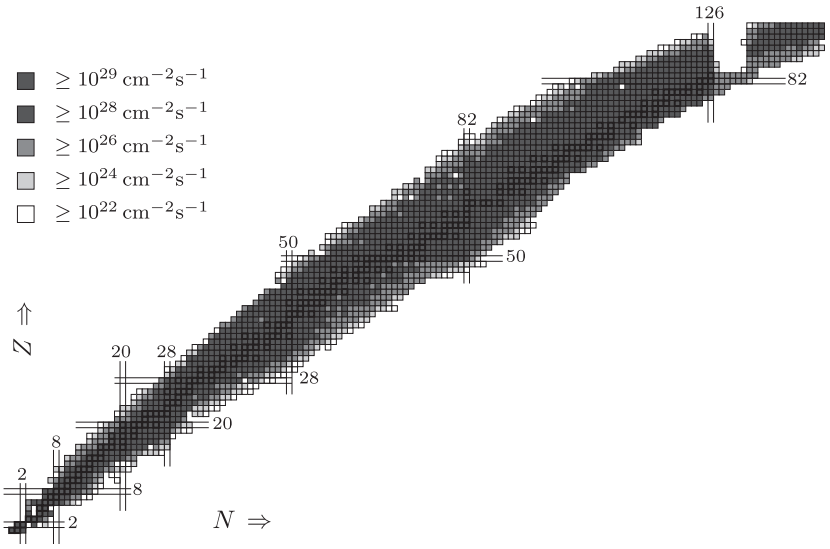

Fig. 4. Maximum achievable luminosities for individual 0.74 GeV/nucleon ion beams at the interaction zone. Shown is the luminosity as function of the charge Z and the neutron number N according to the grey scale code shown in the upper left corner. Stable isotopes and magic numbers are labeled and distinguished by extended lines. A central plateau is visible, which drops rapidly at the edges where the most unstable and short-lived nuclei that can be studied with ELISe are situated. These luminosities comfortably suit to the requirements given in Table 1 for a wide range of isotopes far from the valley of beta-stability. The simulation calculation takes fully into account, (i) production and separation process, (ii) transport through separator and beam lines, (iii) cooling and storage in the storage rings, and (iv) decay losses. For details, see text.

Table 5
Luminosities L for 0.74 GeV/nucleon ion beams for several reference nuclei. Here, $T_{1/2}$ is the half-life of the nucleus at rest, τ its total life time, and N the total number of ions stored in the NESR storage ring.

Element	$T_{1/2}$ (s)	τ (s)	N	L ($\mathrm{cm}^{-2}\,\mathrm{s}^{-1}$)
^{11}Be	13.8	35.6	8.3×10^{9}	2.4×10^{29}
^{35}Ar	1.75	4.5	5.9×10^{7}	1.7×10^{27}
^{55}Ni	0.21	0.5	2.0×10^{7}	4.0×10^{27}
^{71}Ni	2.56	6.5	3.8×10^{7}	1.1×10^{27}
^{93}Kr	1.29	3.3	6.2×10^{6}	1.8×10^{28}
^{132}Sn	39.7	68.2	6.5×10^{8}	1.9×10^{28}
^{133}Sn	1.4	3.5	6.9×10^{6}	2.0×10^{26}
^{224}Fr	199	59.2	3.0×10^{8}	8.6×10^{27}
^{238}U	10^{17}	60	3.4×10^{8}	1.0×10^{28}

in the Super-FRS via the expression:

$$(x|\delta_m) = -\frac{D_i}{M_i}\cdot\frac{d}{r_i}\cdot\frac{L_m}{\lambda} \tag{9}$$

where $(x|\delta_m)$ is the variation of the position with ion mass, e.g. on a slit system, D_i denotes the dispersion, M_i the magnification and d/r_i the normalized degrader thickness for a given stage of the separator. The quantity L_m/λ relates to the stopping power of the degrader material. The degrader thickness is then optimized with respect to the losses expected from electromagnetic dissociation and nuclear reactions in the degrader material with an iterative procedure. The total electromagnetic dissociation cross-section is approximated using a model where particular nuclei disintegrate via excitation to their giant dipole resonance (GDR). The GDR resonance energy is taken from a parameterization [28] that is based on experimental data. To calculate the cross-section, we use 120% of the Thomas–Reiche–Kuhn sum rule and the computed number of virtual E1-photons. For that, the minimal impact parameter b_{min}, which is also used to estimate the nuclear cross-section, is obtained from the systematics [74] by Benesh et al.

(ii) Subsequently, the transport and injection efficiency into the CR-ring is taken into account by using a parameterization that is extracted from various ion-optical simulation calculations [75] and depends on production process, mass, and charge of the secondary beam particle.

(iii) Finally, nuclear and atomic life times are taken into account in order to provide a reliable prediction of the number of cooled ions in the NESR storage ring. Cooling and preparation of ions in the NESR is designed to take place in at most two synchrotron (SIS100/300) cycle times, i.e. within 1.3 or 2.6 s. The nuclear losses have been computed taking the information available from the Lund/LBNL [76] database. The appropriate time dilation is taken into account. For longer-lived ions (10 s to minutes) it is possible to further increase intensity by stacking, i.e. injecting several cycles from the synchrotron into the storage ring in case the production yield is limiting the number of stored ions. Different stacking methods and associated parameters are still being studied [77] and have not yet been included into the simulation calculation.

(iv) Atomic processes in the storage ring, when ions interact with electrons of the electron cooler and the rest-gas, are another important source of losses to be taken into account. Electron capture from the electron cooler in particular radiative recombination for fully stripped ions and the recombination processes (Non Resonant electron Capture, NRC and Resonant Electron Capture, REC) due to interaction with rest-gas electrons can be calculated [78–80] with good precision. Losses also occur when the charge state and, therefor, the magnetic rigidity of the ions change so that they fall outside of the acceptance of recirculating ions. The total life time τ in the ring is given by

$$\frac{1}{\tau} = \frac{1}{\tau_{\mathrm{nuclear}}} + \frac{1}{\tau_{\mathrm{atomic}}} \tag{10}$$

where τ_{nuclear} is the nuclear lifetime, see (iii), and τ_{atomic} is the atomic lifetime. Numerical values for τ for selected isotopes can be found in Table 5.

4.2. Physics performance: elastic scattering

As an example what can be achieved with ELISe, the results of two simulations are shown in Fig. 5 for two the stable nuclei, ^{12}C

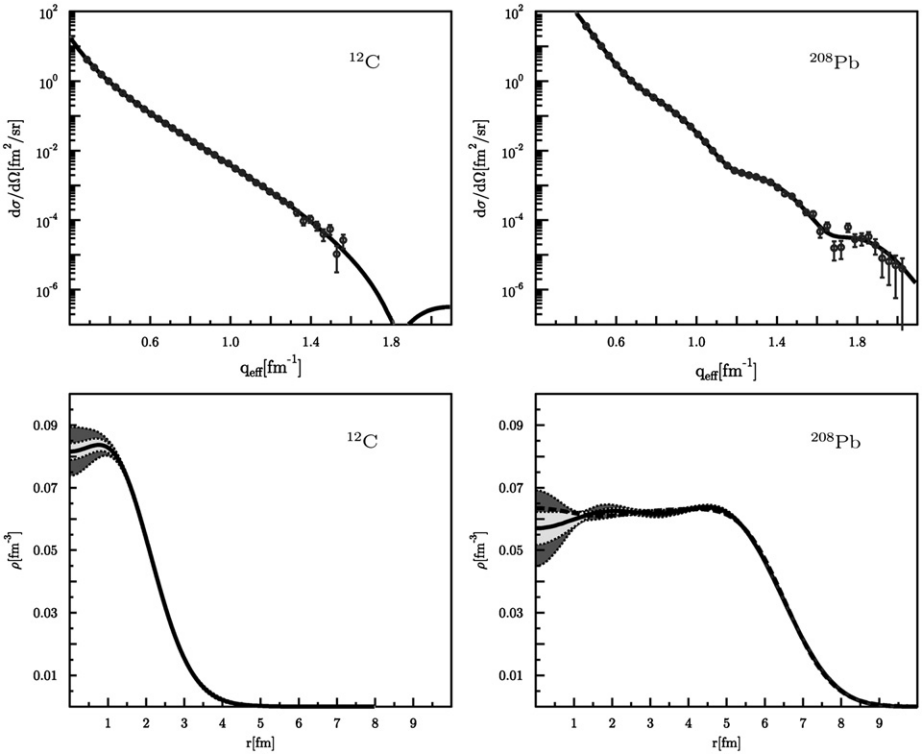

Fig. 5. Results of the simulations for two hypothetical measurements to obtain the charge–density distributions of ^{12}C and ^{208}Pb with a luminosity of 10^{28} cm^{-2} s^{-1}, a solid angle of 100 msr and a running time of 4 weeks. The curves in the upper panels present the "true" cross-sections obtained from the known parameters. The data are simulated data points generated around the curve with their statistical errors. In the lower panels, the corresponding charge–density distributions (solid curve) obtained from the simulated data are shown with the corresponding error bands. The dashed curve in the lower-right panel shows the initial charge distribution for reference. For the carbon case both curves are indistinguishable. See text for further details.

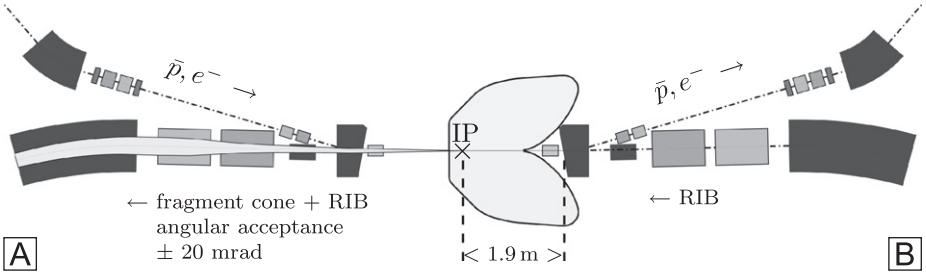

Fig. 6. Interaction zone with the interaction point IP in the bypass section of the NESR. The labels A and B correspond to those in Fig. 2. The bore holes along the beam axis for the viewports in the large dipole stages have been omitted in the drawing. Fragments emerging from the interaction zone are transported to a 7 m long straight section after the dipole (at position A) providing a sufficiently long time-of-flight path for the in-ring detectors system (see Section 6).

and ^{208}Pb, which have very large differences in their charge–density distributions.

The Fourier–Bessel parameters with which the "true" cross-sections are calculated are taken from Ref. [31]. These cross-sections were obtained with the code MEFCAL [81] that uses a distorted-wave approach. They were subsequently randomized with the expected statistics for a 4 week run, and with a luminosity of 10^{28} cm^{-2} s^{-1} assuming a solid angle of 100 msr to obtain the "experimental" data points shown in the figure. These points were then fitted using the code MEFIT [81]. The output of this code is the parameters of the charge–density distribution. In the fit, an exponential fall-off as upper limit for the cross-section outside the measured region was assumed.

The inner-shaded areas in the lower panels of the figure result from the "statistical" uncertainties of the measurement and the outer-shaded areas represent the fact that one does not measure to infinite momentum transfers and thus creates an error in the Fourier transform. The results of the fit (solid curve) can be compared directly with the original distributions used to generate the "data" (dashed curve). As can be seen in the figure, with a modest solid angle of 100 msr, a running time of 4 weeks, and a luminosity of 10^{28} cm^{-2} s^{-1}, one can already have results for charge–density distributions which can be compared to results of theoretical models.

The sensitivity of the simulated experiment indicated by the given error band should be compared to the theoretical predictions presented by Grasso et al. [14], where e.g. a central depletion by 50% in the nucleus ^{34}Si is expected due to its particular nuclear structure. The shown result would clearly allow to confirm or abandon such a forecast.

4.3. Bypass design

The bypass region is shown in detail in Fig. 6. The arrangement of magnetic elements is symmetric with respect to the interaction point. The first two dipoles are placed symmetrically around the

IP at a distance of 1.9 m, leaving enough space for installing the electron spectrometer. Both are used to separate the orbits of ions and electrons. As electrons and ions have opposite electric charges and move in opposite directions both orbits are deflected to the left by the separation dipoles. The magnetic field in the dipoles has to be adapted to the energy of the electron beam in order to bend the electrons to a fixed angle (16.5°) before entering the EAR. The bending angle for ions depends on the ion-beam energy and varies between 0.8° and 3.0°. Just in front of the bending magnets two pick-up systems are installed in order to measure the beams orbits. Two additional dipoles are placed exclusively in the ion path, allowing for an orbit correction depending on the particular electron and ion beam energies. The following quadrupole doublets combine the beta-functions in the IP and in the ring and focus into the adjacent large dipole stages. These subsequently bend the ions by 15°, and eventually, the ion trajectory unites with the original ion orbit in the NESR.

The bypass is exclusively used in the collider mode. In this case, as shown in Fig. 12, the two last NESR magnets of NESRs dipole triplets in the arcs are switched off in order to direct the ions into the bypass region. The straight sections connecting the NESR with the EAR provide about 7 m of free space. The section before the interaction zone at position [B] in Fig. 6 will be used to install an additional RF-cavity exclusively used for the preparation of bunches for the collider mode. The section following position [A] is part of the in-ring spectrometer setup described in Section 6.

5. Electron spectrometer

5.1. Challenges to be met

The technological challenge for the eA collider results from the simultaneous requirement for large acceptance and high momentum resolution. In addition, the spectrometer should allow for tracking the position of the reaction vertex inside the reaction zone. Existing magnetic spectrometers only partially fulfill these specifications. For instance, the electron spectrometers at the universities of Darmstadt [82] and Mainz [83] and at the research center TJNAF [84] meet the requirements with respect to momentum and angular resolution. They can handle reaction zones extending up to 10 cm, but only have a moderate acceptance of <40 msr.

Existing toroidal and solenoidal spectrometers, e.g. HADES [85], BLAST [86] and BELLE [87], that cover 2π in azimuthal angle ϕ, provide the required acceptance but only modest resolution. The main limitations for the resolution arise from energy and angular straggling of electrons in the tracking detectors. A large-acceptance spectrometer has advantages, but further research and development are needed for a suitable design, which can satisfy both experimental requirements as discussed above. Due to the fact that differential cross-sections for electron scattering decrease rapidly with the angle of the scattered electron, an ideal electron spectrometer should cover 2π in azimuthal angle but needs to provide a moderate acceptance in scattering angle of about $\theta=10^{\circ}-20^{\circ}$ only. The considerations have shown that magnetic dipole-based spectrometers designed for the collider with an acceptance up to about 100 msr can be built at a reasonable cost [88].

5.2. Large-angle dipole spectrometer

5.2.1. Spectrometer with large azimuthal acceptance

The restricted luminosity of the collider can be partially compensated by a large acceptance of the electron spectrometer. We consider first a spectrometer with an extraordinarily large azimuthal acceptance, being compared to typical magnetic spectrometer installations. A spectrometer consisting of two quadrupoles and one dipole (QQD type) is a promising candidate for this purpose. The layout for such a spectrometer is shown in Fig. 7. The first quadrupole magnet with large aperture is located as close as possible to the IP.

The rectangular aperture of the first quadrupole magnet is 72 cm in vertical and 24 cm in horizontal direction. The field gradient is 8.1 T/m. Because of the very high current density (≈ 70 A/mm^2) reached, the coils have to be super-conducting. A very large acceptance in vertical angles $\approx \pm 34^{\circ}$ is achieved due to the strong vertical focusing force of the quadrupole. However, the first quadrupole magnet defocuses the horizontal motion. In order to compensate this effect, a second quadrupole magnet focusing horizontally and defocusing vertically is installed. This quadrupole magnet is a normal-conducting type with a field gradient of about 1.7 T/m. The dipole magnet placed downstream from the two quadrupole magnets analyzes the scattered electron momentum. For an arbitrarily chosen bending angle of the dipole magnet, the electron rays can be focused both horizontally and vertically at the focal plane by tuning the strengths of the quadrupole magnets.

The result of a ray-tracing calculation is shown in Fig. 7: 27 rays with three magnetic rigidities (1.9, 2.0, and 2.1 Tm), for three horizontal angles (+4°, 0°, and −4°) and three vertical angles (+34°, 0°, and −34°) are shown. The acceptance exceeds 1200 mrad for the central momentum, but it is smaller at both edges of the momentum range. The horizontal angular acceptance is about 200 mrad. The spectrometer, as shown in Fig. 7, is optimized for measurements around a scattering angle of 90°, but can also be rotated around the IP to cover smaller angles. In order to allow measurements at smaller scattering angles, the first quadrupole magnet is made as slim as possible. For these requirements, a super-conducting Panofsky magnet, employing current sheets bound by iron, rather than shaped pole faces to establish the field, is the most suitable selection. A quarter of the first

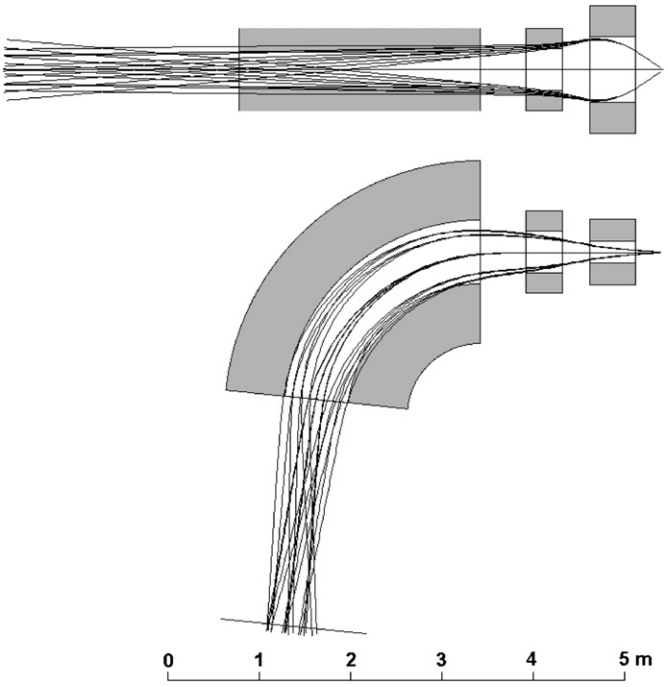

Fig. 7. Side view (top) and top view (bottom) of the QQD-spectrometer with large azimuthal acceptance.

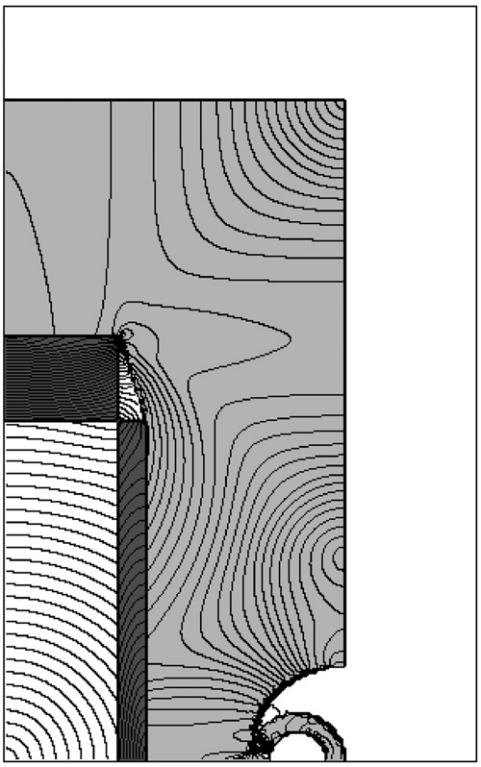

Fig. 8. Three-dimensional magnetic field calculation for the first super-conducting Panofsky quadrupole of the QQD-spectrometer with large azimuthal acceptance. Contours of the field strength are shown in 0.1 T steps. The quality of the quadrupole field is demonstrated by their equidistant and concentric appearance.

quadrupole magnet is shown in Fig. 8. The trimming of the side yoke is shown, which provides space for the beam pipe when QQD spectrometer is set at the minimal scattering angle of 50°. The most forward angle achievable with the QQD spectrometer depends on a compact magnetic shield. In the considered design, two cylindrical layers of magnetic shield cover the vacuum pipe of the colliding beams. The outer and inner radii of the shield are assumed to be 40 and 20 mm, respectively. The outer and inner shell thicknesses are then 13 and 5 mm, respectively. The shield suppresses the penetration of magnetic field through the side yoke of the magnet. A two-dimensional calculation shows that the detrimental magnetic field along the beam line is most serious at the front face of the quadrupole magnet where the conductor is not shielded by the yoke of the magnet in contrast to the side face. Without magnetic shield, the magnetic flux density at the nearest position to the pipe was calculated to be about 0.4 T. With the double-layered cylindrical shield, the field strength could be reduced to a safe value of about 0.003 T.

The performance of the spectrometer can be summarized as follows:

- The spectrometer provides an extraordinarily large vertical angle acceptance of 1200 mrad.
- The acceptance in horizontal angle is about 200 mrad.
- The spectrometer can be used for measurements in a range of scattering angles from about 50° to more than 100°.

Selected properties of the magnetic elements are given in Table 6.

5.2.2. Spectrometer with a large range of scattering angles.

The second, more versatile system under consideration is an electron spectrometer composed of a deflection magnet (DM)

Table 6
Some properties of the elements for the QQD spectrometer with large azimuthal acceptance.

First quadrupole magnet			
Horizontal aperture	24 cm	Vertical aperture	72 cm
Yoke width	72 cm	Yoke height	140 cm
Length	50 cm	Field gradient	8.1 T/m
Second quadrupole magnet			
Bore diameter	46 cm	Field gradient	1.7 T/m
Length	40 cm		
Dipole magnet			
Gap	38 cm	Bending angle	84°
Mean orbit radius	180 cm	Magnetic field	1.0 T

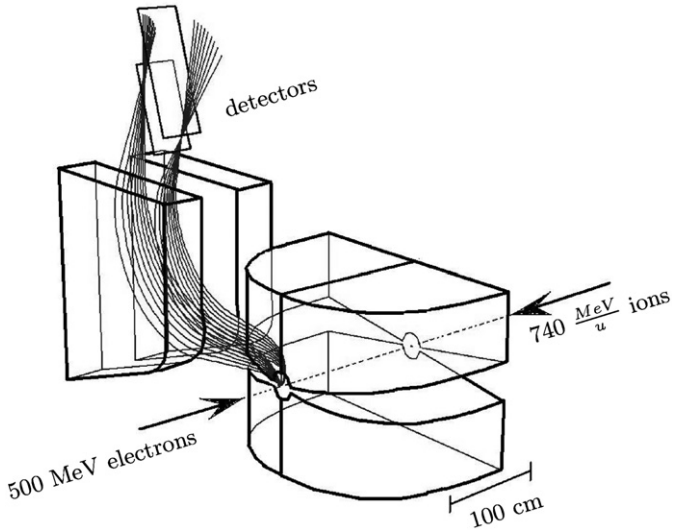

Fig. 9. Schematic view of the electron spectrometer consisting of a pre-deflection magnet and a vertical-dipole spectrometer. Trajectories are shown for 500 MeV electrons elastically scattered off 0.74 GeV/nucleon, $A=100$ ions with a momentum transfer of 400 and 600 MeV/c (43.91° and 62.82°), respectively. The focal plane detectors are located outside the vacuum chamber of the magnet system.

where two vertical dipole magnets (VM) can be placed symmetrically on both sides of the DM. The spectrometer is schematically shown in Fig. 9 (only one VM is shown in this figure). The DM magnet can be seen as a pair of dipoles with an opposite magnetic field that are coupled together. The DM acceptance in vertical angle is ± 150 mrad. The specific shape of DM ensures a deflection of the scattered electron in the horizontal plane towards $\approx 90^\circ - \theta_{e'}$, i.e. perpendicular to the beam axis, for scattering angles $\theta_{e'}$ ranging from about 10° to 60°. The inner regions can be kept field free by appropriate shielding to avoid interference with the circulating beams. Initially the pre-deflection system (DM) will be followed by the vertical dipole spectrometer (VM) at the side of the DM facing inside the EAR. Electrons that are elastically scattered to the same polar angle but with different azimuthal angles are focused in the focal plane of the spectrometer. Calculated trajectories for 500 MeV electrons elastically scattered off a 0.74 GeV/nucleon, $A=100$ ion, with transferred momenta of 400 and 600 MeV/c (43.91° and 62.82°), and assuming a 2 T field and a gap width of 25 cm for the VM, are shown in Fig. 9. The VMs is equipped with two-dimensional coordinate detector systems and a scintillator array. All detectors and foils are located outside the vacuum chamber of the magnet system in order to minimize distortions from straggling.

Full three-dimensional Monte Carlo simulations have been performed to estimate the achievable resolution of the proposed spectrometer. The calculations were made in two steps. During

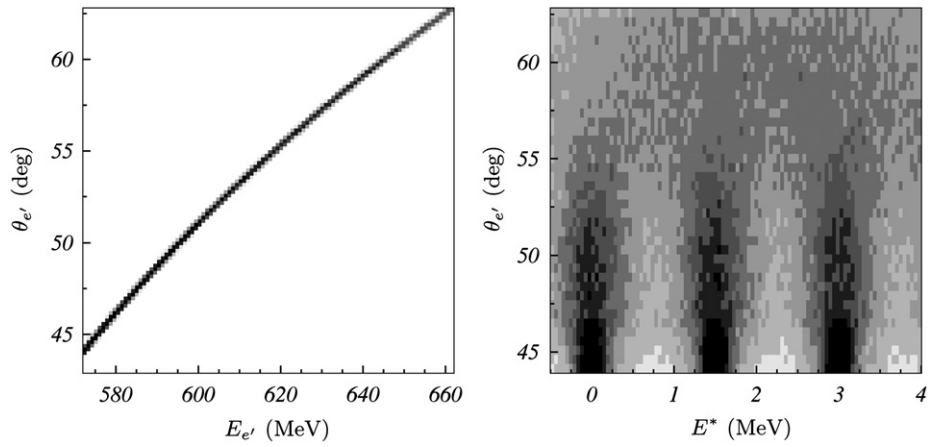

Fig. 10. Left panel: Angle versus energy-range covered for a particular setting of the vertical dipole. The curve is obtained in Monte Carlo simulations where 500 MeV electrons scatter off 0.74 GeV/nucleon ions with $A=100$. Elastic and inelastic ($E^*=1.5$, 3.0 MeV) scattering events contribute to the observed seemingly unresolved line. The presented range in scattering angles poses the worst case scenario for reconstructing the excitation energy. Right panel: Polar angle dependence of the recovered excitation energy. A back-tracking routine was used for the reconstruction. Distortions due to momentum spread in the beam, finite beam size, straggling effects and position resolutions of the detectors are present.

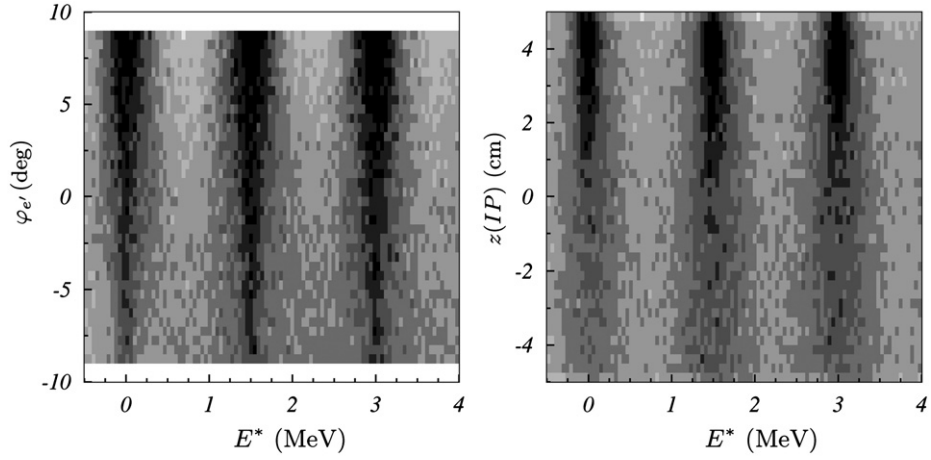

Fig. 11. Left panel: Dependence of the reconstructed excitation energy on azimuthal angle. Right panel: Dependence of the reconstructed excitation energy on the position of the interaction point. Parameters of Monte Carlo calculations are the same as in Fig. 10. The picture shows a clear dependence of the achievable E^* resolution on $z(IP)$ position and $\varphi_{e'}$ angle.

the first stage, electron trajectories were generated according to the design parameters for momentum spread and beam size of the electron beam. Aiming at a pure characterization of the spectrometer no cross-sections were taken into account in the simulations. The coordinates of electron-trajectory intersections with the detector planes were subsequently determined. The obtained hit coordinates were distributed randomly according to the response function of the detectors also including the angular and energy straggling of electrons in the materials. These results were stored as sequential vectors. The vectors were then used as input for the second stage where a back-tracking routine was applied in order to reconstruct the electron energy $T_{e'}$, the polar angle $\theta_{e'}$, the azimuthal angle $\varphi_{e'}$ and the position of the interaction point along the z-axis $z(IP)$. For this procedure, the x and y-coordinates of the interaction point were taken to be zero. Further simulations have shown that the result remains nearly the same if the small transverse extent of the electron beam (see Table 4) is also taken into account. The result of these studies is that all parameters $T_{e'}$, $\theta_{e'}$, $\varphi_{e'}$ and $z(IP)$ can be reconstructed with satisfying accuracy from the four parameters of the hits in the two planes of focal-plane detectors. These results are shown in Figs. 10 and 11 for the case of a large momentum transfer (between 400 and 600 MeV/c) where the kinematics for colliding beams is most unfavorable for the reconstruction.

Disentangling elastic and inelastic scattering in colliding beam kinematics is challenging. The angular range of electrons passing through the VM is about 20° for energies between 560 and 660 MeV. The difficulty is to resolve the peaks separated by only a few hundred keV. This is illustrated in Fig. 10 (left panel) where the thickness of the displayed line is determined by the energy difference of electrons scattered elastically or inelastically with $E^*=1.5$, 3.0 MeV.

In order to account for the extent of the interaction zone $\sigma_z \approx 5$ cm, the first two-dimensional coordinate detector is put in the plane where the trajectories with different azimuthal angles constitute a focus for a given polar angle. The second detector is placed in parallel to the first detector at a distance of 50 cm. The spatial resolution of the first detector is assumed to have a Gaussian distribution with a standard deviation of 50 μm. This detector and the separation foil result in an angular straggling of 1 mrad. The resolution of the detector at the second plane is taken to be 100 μm. The calculations demonstrate the possibility to satisfy all experimental requirements with this spectrometer setup (see also Fig. 11).

5.3. Coordinate detectors

The use of coordinate detectors based on straw tubes [89] has several advantages. Cross-talk is minimized, since the cells are isolated from each other. A channel with a broken sense wire can easily be switched off without turning off all channels. Straw tubes can be designed to withstand pressure and can be placed in vacuum. The inner pressure not only keeps tubes round and inflexible but also results in better resolution. The resolution of tracks is almost independent of the incident angle and angular corrections are not necessary when the drift distance is calculated from the drift time, as with usual drift chambers.

A prototype straw-tube assembly has been built and put into operation at the GSI detector laboratory. The prototype design is based on Kapton tubes covered with a 0.2 μm aluminum layer. The tubes are 60 cm in length and feature a 7.5 mm inner diameter and a total tube-wall thickness of 126 μm. The tubes are filled with Ar/CO_2 (80%/20%) at atmospheric pressure and operate at 1850 V. Detailed studies are currently in progress. Straw tubes filled with quench gases can be operated at even higher pressure (≈ 4 atm) and a higher voltage (≈ 4 kV); see Ref. [90]. Saturated streams in this mode are initiated with high efficiency by a single electron with a gain factor of about 5×10^5. The achieved average spatial resolution of a single tube is 50 μm [90].

The second position-sensitive detector system under consideration is the use of vertical drift chambers instead of two layers of x, y-coordinate detectors. These chambers allow to measure two coordinates of the electron trajectory crossing the detector plane (x, y) as well as polar and azimuthal angles (θ,ϕ) of the electron trajectory. Existing chambers provide a resolution close to the requirements: $\delta x < 100$ μm, $\delta y < 200$ μm, $\delta\theta < 0.3$ mrad, $\delta\phi < 1$ mrad. Such a system is routinely used at the MAMI facility [91] and at TU Darmstadt. Therefore, the already existing designs could be easily adapted to meet the requirements of the ELISe experiment.

It is foreseen to place a plastic scintillation system after the focal plane of the spectrometer. This system consists of two modules (plastic scintillation bars, $120 \times 10 \times 4$ cm^3) viewed by two photomultiplier tubes from opposite sides coupled with optical pads to the attached light guides. The expected intrinsic time resolution will thus be about 0.1–0.2 ns. The bunch timing signals of the NESR will be used for time-of-flight measurements. It is already sufficient to use only one module to detect scattered electrons. The second module is introduced in order to decrease background. The scintillation bars can be manufactured from NE-102 material. Such systems have been successfully used in different experiments to measure electrons with high efficiency and good timing resolution [92].

6. In-ring detectors

The detection of reaction products is another task required of the ELISe facility. A detector setup placed behind the straight bypass section (A–B, see Fig. 2) using the first bending dipole as spectrometer magnet for heavy ions is foreseen to be used for this task. The detectors will operate in coincidence with the scattered electrons. They will allow to disentangle different reaction channels in the case of inelastic scattering experiments (e.g. excitation of particle unstable states, quasi-free scattering, electro-fission) and provide means to clean the electron energy spectra from radiative tails originating from other reaction channels.

Cooled heavy-ion beams circulate in the NESR with a momentum spread of $\Delta p/p \approx 10^{-4}$ and with an emittance of about 1π mm mrad. The design and settings of the magnetic devices are thus governed by the requirement to keep a high-quality ion beam stored. Therefore, the degrees of freedom in building a large acceptance system for the ions emerging from the interaction zone are rather limited. The current design for the bypass shown in Fig. 6 allows for the detection of fragments in a ± 20 mrad cone which is sufficient for performing the most demanding electro-fission experiments, thanks to the kinematical forward focusing.

A possible version of the in-ring detector layout is shown in Fig. 12 together with trajectories calculated for fragments with different magnetic rigidities in steps of 1%.

- The detector array at position 1 in Fig. 12 allows for the reaction tagging by particle identification for ions (e.g. (e,e′n) via (e,e$^{\prime A-1}$Z)).
- The two arrays at positions 2 and 3 provide in addition a fragment tracking with moderate momentum resolution (by time-of-flight measurements, and with an acceptance $\Delta B\rho/B\rho \approx \pm 7\%$). The obtained resolution is high enough to identify also fission fragments with their large momentum spread.
- The detector array at position 4 implements the same tasks with even better resolution but further reduced acceptance.

Simulation calculations show that a resolution of $\Delta p \approx 20$ MeV/c, corresponding to about 0.5 MeV missing energy resolution, can be achieved for both longitudinal and transverse momenta in the case of quasi-free scattering (e,e'p) for a 500 MeV electron

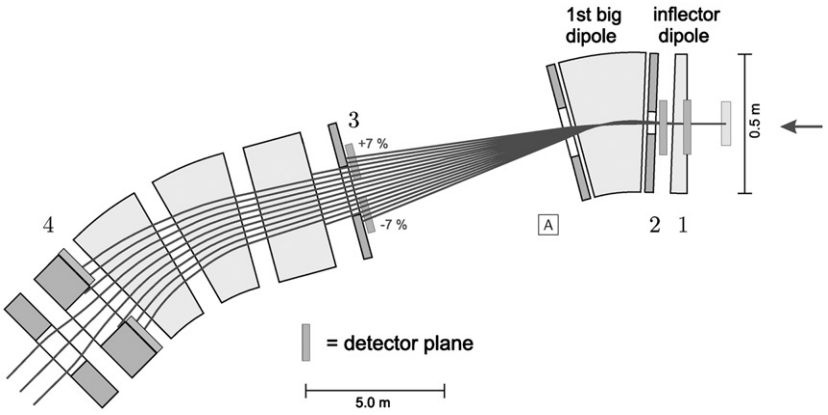

Fig. 12. Ion trajectories calculated for different magnetic rigidities through the first bending and adjacent straight section behind the interaction zone. These trajectories are shown for seven steps of 1% deviation in magnetic rigidity in positive and negative directions from the nominal magnetic rigidity of the circulating beam, respectively. Label A refers to the position shown in the previous setup Figs. 2 and 6.

beam interacting with 740 MeV/nucleon oxygen isotopes. In addition, a time-of-flight resolution of 35 ps FWHM is needed to separate fission fragments by mass reliably. First measurements have shown, that this time resolution can be reached by using quenched scintillator material viewed with fast photomultipliers.

Detectors located near the circulating beam in the first two planes (1 and 2 in Fig. 12) should be UHV compatible and should be thin enough in order to avoid distortions caused by multiple scattering inside the detector material. The first choice is an array of 100 μm thick CVD (chemical vapor deposition) diamond microstrip detectors. Alternatively, 100 μm thick silicon detectors would also meet the requirements, however, they are more sensitive to irradiation. Both detector types can provide 0.1 mm resolution for the ion hit positions. Compared to Si-based detectors, a diamond detector has excellent merits in terms of high radiation resistance, low leakage current, high operation temperature and high chemical inertia. The expected resolutions for these assemblies are $\Delta p/p \approx 10^{-3}$ and 1 mrad for the momentum and angle measurements, respectively, in accordance with the previously shown example.

Since the detectors can only be positioned after the beam preparation during setup or cooling phase in the NESR is completed, the detector arrays are subdivided into two parts, each one mounted on a remotely controlled driving device. They are designed to be removable in vertical direction and the range is kept adjustable according to the beam emittance. Scattered ions can then be detected starting from a minimum scattering angle of about 1 mrad.

A halo around the ion beam stored in the NESR could potentially damage the detectors. Another source of radiation are beam ions leaving the orbit after scattering off the counter-propagating electrons or ions that undergo atomic charge–changing reactions in the rest-gas. Calculations have shown that for a luminosity of 10^{29} cm^{-2} s^{-1} the count rate, normalized to the detector area, will not exceed 10^4 cm^{-2} s^{-1} for detectors placed at a distance of 10 mm from the NESR beam axis. This estimate means that neither the diamond nor the silicon detectors will show any essential damage even after three years of continuous operation.

The existing experimental storage ring (ESR) at GSI is equipped with gas detectors, scintillators, silicon-strip detector arrays, and diamond detectors. The experience obtained during operation of ESR will be used and existing techniques will be extended to satisfy the specific demands of the eA collider.

7. Luminosity monitor

Elastic electron scattering is always accompanied by the process of bremsstrahlung, involving emission of photons. A radiative tail of lower-energy electrons appears in the electron energy spectrum, e.g. due to bremsstrahlung, leading to an extension of the electron energy spectrum below the elastic scattering peak [93]. Bremsstrahlung is therefore commonly used to monitor luminosity. The angular and energy distributions of the bremsstrahlung are shown in Fig. 13. The narrow angular distribution ($\Delta\theta_\gamma \approx 1/\gamma_e$ rad) allows for diagnostic and adjustment of the electron beam position.

The presence of rest-gas in NESR, even on a level of 3×10^{-11} mbar, is a source of $500N_\gamma$/s background bremsstrahlung of photons with energies larger than 100 MeV for the electron-beam parameters given in Table 4. As can be seen in Fig. 13 in panel 2, the effect of screening by orbital electrons leads to strong changes in the bremsstrahlung spectrum. This effect allows in principle for a correction for the rest-gas background contribution by precise measurements of the shape of the γ-spectra. Bremsstrahlung intensities of γ-rays with energies larger than 100 MeV are given in Table 7 for several reference nuclei with a kinetic energy of 0.74 GeV/nucleon. In this table, L_B denotes the luminosity where the γ-ray background due to the rest-gas becomes equal to the amount of bremsstrahlung caused

Table 7
Bremsstrahlung intensity for γ-rays with energies higher than 100 MeV (ion beam kinetic energy 0.74 GeV/nucleon). Here, σ_B is the cross-section for producing bremsstrahlung at the given conditions, and L_B is the value where the γ-background caused by rest-gas in the storage ring becomes equal to the amount of bremsstrahlung induced by the ion beam.

Ion beam	Luminosity (cm^{-2} s^{-1})	σ_B (barn)	Yield N_γ (10^3 s^{-1})	L_B (cm^{-2} s^{-1})
^{11}Be	2.4×10^{29}	0.48	115.2	1.1×10^{27}
^{35}Ar	1.7×10^{27}	9.7	16.5	5.3×10^{25}
^{55}Ni	4.0×10^{27}	23	94.1	2.2×10^{25}
^{71}Ni	1.1×10^{27}	23	25.9	2.2×10^{25}
^{93}Kr	1.8×10^{28}	38	700	1.3×10^{25}
^{132}Sn	1.9×10^{28}	75	1425	7.0×10^{24}
^{133}Sn	2.0×10^{26}	75	15.0	7.0×10^{24}
^{224}Fr	8.6×10^{27}	227	1953	2.3×10^{24}
^{238}U	1.0×10^{28}	254	2539	2.0×10^{24}

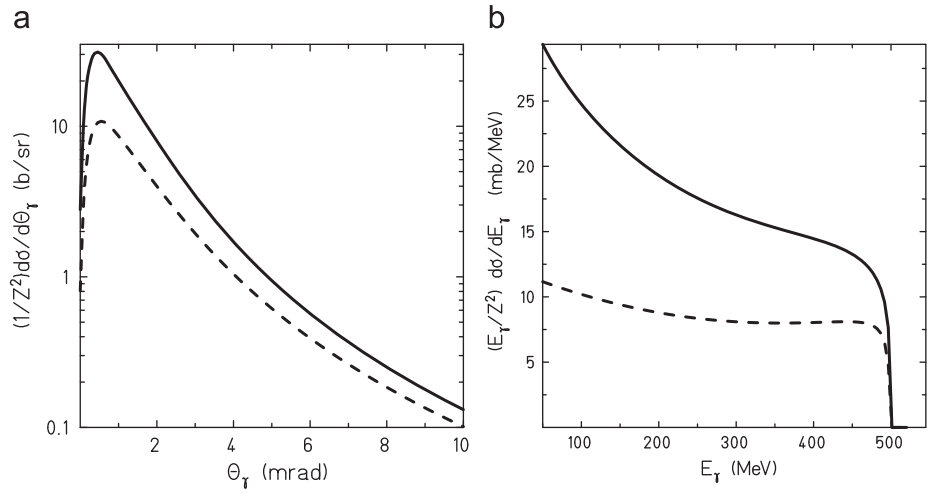

Fig. 13. Angular (panel a) and energy (panel b) distributions of bremsstrahlung emitted by the electron beam. The distributions are given for scattering off 0.74 GeV/nucleon ions (solid curve) and on rest-gas nuclei (dashed curve). In the latter case, the effect of the screening of the nucleus by atomic electrons is taken into account.

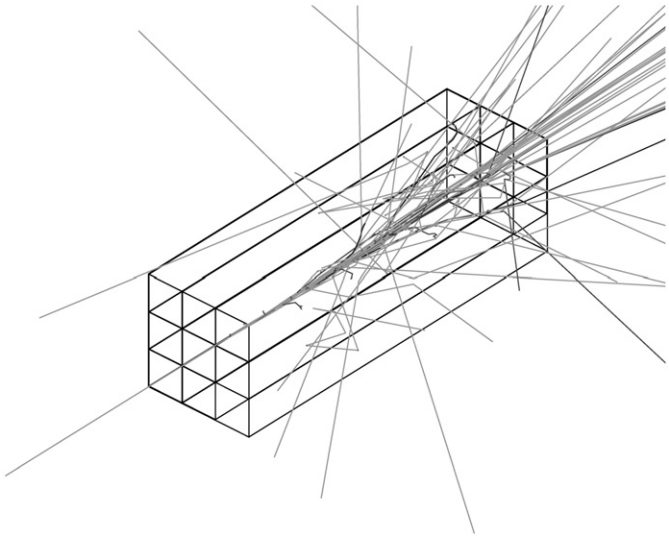

Fig. 14. Shower created in a stack of 3×3 $PbWO_4$ crystals by one 300-MeV-gamma ray (GEANT4 simulation calculation). The geometry used for the calculations is the same as described in the text.

by the presence of the ion beam. We neglect the ionization of the residual gas in the vacuum chamber by the circulating electron bunches. The ionization creates positive ions which under certain circumstances become trapped in the potential well of the stored electron beam [94]. The effect is suppressed due to the counter-propagating beam of positive ions moving along the same trajectory.

For the luminosity measurement using bremsstrahlung a system capable of detecting high energy photons is needed. The $PbWO_4$ crystal is distinguished by its fast decay time (6/30 ns at 440/530 nm), a high density (8.28 g/cm^3) and its radiation hardness. Thus, it is an excellent γ-detector also due to its favorable optical, physical and chemical properties, accounting for its long-term stability. The radiation length (x_0) of the crystal is less than 1 cm, where x_0 is linked to the total energy loss $E(x)$ by $E(x)=E_0\exp(-x/x_0)$. A material thickness corresponding to $20x_0$ is sufficient to absorb about 99% of the induced showers. The crystals are characterized by a very small Molière radius (≈ 2 cm) which describes the transverse extension of the showers due to multiple scattering of low energy electrons inside the material. More than 99% of the shower is situated within 3 Moliere radii bounds. The application of these detectors for γ-spectroscopy from tens of MeV up to several hundred MeV with good energy ($\sigma_E/E=(1.7/\sqrt{E\,[\mathrm{GeV}]}+0.6)\%$) and spatial resolution ($\sigma_{x,y}\leq 5$ mm) is feasible [95].

The luminosity monitor will be built as a 3×3 matrix of $PbWO_4$ scintillators ($20\times20\times200$ mm^3), and placed about 8–10 m from the interaction point (see Fig. 2, C). The bremsstrahlung beam then illuminates mainly the central cell of the matrix. The detector array covers the dominant part of the radiation cone. A simulated shower created by one 300-MeV-gamma ray is shown in Fig. 14. An Avalanche Photo Diode (APD) readout is currently foreseen which achieves a suitable energy resolution, if the diode is being cooled down to a well stabilized ($\Delta T=0.1\ ^\circ$C) temperature.

8. Data acquisition and handling

There are several specific demands on the ELISe data acquisition and online analysis, as the experiment is an integral part of the NESR/EAR accelerator complex. The detection system in the ELISe experiment will be used to monitor the achieved beam quality, and to optimize the beam settings accordingly. A strong coupling to the accelerator control system requires stable operation of the detector systems with their associated slow-control components and online analysis. Furthermore, it is mandatory that these systems can be operated without detailed knowledge about their components by the accelerator staff. Since ELISe will act as a data source for the accelerator controls, we foresee strict compliance to the given interfaces and timing definitions and will provide pre-analysis, e.g., profile, luminosity and emittance information.

At the same time, the experimental data treatment will require complete event-wise data recording at the highest possible rates in the electron tracking system. The tracker will be read out by dedicated front-end electronics (e.g. Ref. [96]) coupled to a flexible (FPGA, DSP, CPU based) readout system that will perform the first analysis steps online. In such a way, a considerable data reduction coming from this fixed installation within the experiment can be achieved. We plan to run a trigger-less, data-driven system. The front-end acquisition system will also allow for further data and background reduction by using local trigger information in order to define regions of interest in the data stream. The concept for the actual data readout, event building, transfer and long-term storage is based on a scalable and standardized system (e.g. Ref. [97]) provided by GSI/FAIR, see also Ref. [98].

9. Summary

The proposed electron–ion collider will provide a unique experimental facility for FAIR. The ELISe experiment is part of the core program [99] of the FAIR facility.

It becomes feasible due to the intense pulsed beams from the FAIR synchrotrons, allowing for an optimized storage ring operation. Luminosity estimates have been presented in this paper and the collider kinematics has been discussed. It turns out that the large center-of-mass energy for the electrons leads to small center-of-mass angles for a particularly chosen momentum transfer. The expected cross-sections are thus sizable and will largely compensate the seemingly poor luminosities achievable for collider experiments.

A major advantage of the ELISe facility, in addition to the analysis of electrons, is the possibility also to fully analyze recoils and target fragments after reactions. They are moving with the stored ion beam towards the first bending section in the ion path following the intersection of the two storage rings. The section is subsequently also used as magnetic spectrometer for the recoils.

The most attractive as well as challenging features of the proposed concept are:

- The ELISe project pioneers electron scattering off radioactive nuclei for nuclear structure studies while making use of well established heavy-ion storage ring techniques.
- The versatile ELISe experiment will consist of three major components (i) an electron spectrometer, (ii) an in-ring detection system, and (iii) a luminosity monitor, which can be extended with additional detectors for specific experiments.
- These basic components have been considered in this paper. They can handle a wide range of different nuclear reactions and thus address numerous physics questions. Kinematically complete measurements where the electrons, the target-like recoils with their associated gammas, are measured with high efficiency are facilitated due to the relativistic focussing (Lorentz boost). This is quite in contrast to conventional fixed-target electron-scattering experiments.
- Technologically, the requirement of high resolution combined with high acceptance for the electron spectrometer is most demanding. Two concepts for the spectrometer have been shown here, and their properties have been discussed.

The conceptual design of a collider experiment for nuclear structure investigations is featured in the present paper. The envisaged solutions fulfil already most of the experimental requirements posed by the physics cases. In the future, a more detailed design of particular components will be presented. The expected gain of information will allow to perform realistic physics simulations, where ELISe's physics performance can be fully explored.

Acknowledgments

The authors acknowledge financial support from the EC via the INTAS programme, Grant nos. 03-54-6545 and 05-1000008-8272. This work has been supported by the US Department of Energy, Office of Nuclear Physics, under Contract No. DE-FG02-91ER-40609. This work was partially supported by the Hessian LOEWE initiative Helmholtz International Center for FAIR.

References

[1] NuPECC Long Range Plan, 2004 〈http://www.nupecc.org/lrp02/long_range_plan_2004.pdf〉; 〈http://www.nupecc.org/pub/NuPECC_Roadmap.pdf〉.
[2] E. Garrido, E. Moya de Guerra, Nucl. Phys. A 650 (1999) 387.
[3] E. Garrido, E. Moya de Guerra, Phys. Lett. B 488 (2000) 68.
[4] S.N. Ershov, Yad. Fiz. 67 (2004) 1877;
S.N. Ershov, Phys. At. Nucl. 67 (2004) 1851.
[5] Z. Wang, Z. Ren, Phys. Rev. C 70 (2004) 034303.
[6] S.N. Ershov, B.V. Danilin, J.S. Vaagen, Phys. Rev. C 72 (2005) 044606.
[7] A.N. Antonov, D.N. Kadrev, M.K. Gaidarov, E. Moya de Guerra, P. Sarriguren, J.M. Udias, V.K. Lukyanov, E.V. Zemlyanaya, G.Z. Krumova, Phys. Rev. C 72 (2005) 044307.
[8] C.A. Bertulani, J. Phys. (London) G 34 (2007) 315.
[9] C.A. Bertulani, Phys. Rev. C 75 (2007) 024606.
[10] C.A. Bertulani, Phys. Rev. C 75 (2007) 057602.
[11] S. Karataglidis, K. Amos, Phys. Lett. B 650 (2007) 148.
[12] E. Khan, M. Grasso, J. Margueron, N. Van Giai, Nucl. Phys. A 800 (2008) 37.
[13] X. Roca-Maza, M. Centelles, F. Salvat, X. Viñas, Phys. Rev. C 78 (2008) 044332.
[14] M. Grasso, L. Gaudefroy, E. Khan, T. Niksic, J. Piekarewicz, O. Sorlin, N. Van Giai, D. Vretenar, Phys. Rev. C 79 (2009) 034318.
[15] Yu.Ts. Oganessian, O.N. Malyshev, I.N. Meshkov, V.V. Parkhomchuk, P. Pokorny, A.A. Sery, S.V. Stepantsov, Ye.A. Syresin, G.M. Ter-Akopian, V.A. Timakov, Z. Phys. A 341 (1992) 217.
[16] T. Katayama, T. Suda, I. Tanihata, Phys. Scr. T 104 (2003) 129.
[17] G. Münzenberg, J. Friese, H. Geissel, I. Meshkov, G. Schrieder, E. Syresin, Nucl. Phys. A 626 (1997) 249.
[18] I. Meshkov, G. Münzenberg, G. Schrieder, E. Syresin, G.M. Ter Akopian, Nucl. Instr. and Meth. A 391 (1997) 224.
[19] L.V. Chulkov, G. Münzenberg, G. Schrieder, H. Simon, Phys. Scr. T 104 (2003) 144.
[20] H. Simon, Nucl. Phys. A 787 (2007) 102.
[21] FAIR—Facility for Antiproton and Ion Research 〈http://www.gsi.de/fair/index_e.html〉.
[22] T. Suda, M. Wakasugi, Prog. Part. Nucl. Phys. 55 (2005) 417.
[23] A. Richter, Nucl. Phys. A 751 (2005) 3c.
[24] B. Jonson, Phys. Rep. 389 (2004) 1.
[25] T.W. Donnelly, J.D. Walecka, Ann. Rev. Nucl. Part. Sci. 25 (1975) 329.
[26] E. Moya de Guerra, Phys. Rep. 138 (1986) 293.
[27] J. Heisenberg, H.P. Blok, Ann. Rev. Nucl. Part. Sci. 33 (1983) 569.
[28] M.N. Harakeh, A. van der Woude, Giant Resonances, Clarendon Press, Oxford, 2001.
[29] D. Drechsel, M.M. Giannini, Rep. Prog. Phys. 52 (1989) 1083.
[30] D.R. Yennie, D.G. Ravenhall, R.N. Wilson, Phys. Rev. 95 (1954) 500 (and references therein).
[31] H. de Vries, C.W. de Jager, C. de Vries, At. Data Nucl. Data Tables 36 (1987) 495.
[32] G. Fricke, C. Bernhardt, K. Heilig, L.A. Schaller, L. Schellenberg, E.B. Shera, C.W. de Jager, At. Data Nucl. Data Tables 60 (1995) 177.
[33] J. Friedrich, N. Voegler, Nucl. Phys. A 373 (1982) 192.
[34] I. Angeli, R.J. Lombard, Z. Phys. A 324 (1986) 299.
[35] J. Friedrich, N. Voegler, P.-G. Reinhard, Nucl. Phys. A 459 (1986) 10.
[36] G.S. Anagnostatos, A.N. Antonov, P. Ginis, J. Giapitzakis, M.K. Gaidarov, J. Phys. (London) G 25 (1999) 69.
[37] M. Bender, K. Rutz, P.-G. Reinhard, J.A. Maruhn, W. Greiner, Phys. Rev. C 60 (1999) 034304.
[38] J. Decharge, J.-F. Berger, K. Dietrich, M.S. Weiss, Phys. Lett. B 451 (1999) 275.
[39] A.V. Afanasjev, S. Frauendorf, Phys. Rev. C 71 (2005) 024308.
[40] W.A. Richter, B.A. Brown, Phys. Rev. C 67 (2003) 034317.
[41] J. Friedrich, N. Voegler, Phys. Rev. Lett. 47 (1981) 1385.
[42] P. Sarriguren, E. Moya de Guerra, A. Escuderos, Nucl. Phys. A 658 (1999) 13; P. Sarriguren, E. Moya de Guerra, A. Escuderos, Phys. Rev. C 64 (2001) 064306.
[43] V.K. Lukyanov, E.V. Zemlyanaya, D.N. Kadrev, A.N. Antonov, K. Spasova, G.S. Anagnostatos, J. Giapitzakis, Part. Nucl. Lett. 2 (111) (2002) 5; V.K. Lukyanov, E.V. Zemlyanaya, D.N. Kadrev, A.N. Antonov, K. Spasova, G.S. Anagnostatos, J. Giapitzakis, Bull. Rus. Acad. Sci. Phys. 67 (2003) 790.
[44] M. Nishimura, E. Moya de Guerra, D.W.L. Sprung, Nucl. Phys. A 435 (1985) 523;
J.M. Udias, M.Sc. Thesis, Universidad Autonoma de Madrid (unpublished), 1987.
[45] T. de Forest Jr., J.D. Walecka, Adv. Phys. 15 (1966) 1.
[46] G.D. Alkhazov, V.V. Anisovich, P.E. Volkovyckii, Diffractional Interaction of Hadrons with Nuclei at High Energies, Nauka, Leningrad, 1991, p. 94.
[47] V.V. Burov, V.K. Lukyanov, Preprint JINR (1977) R4-11098, Dubna; V.V. Burov, D.N. Kadrev, V.K. Lukyanov, Yu.S. Pol', Phys. At. Nucl. 61(4) (1998) 525.
[48] J. Friedrich, Th. Walcher, Eur. Phys. J. A 17 (2003) 607.
[49] G.G. Simon, Ch. Schmitt, F. Borkowski, V.H. Walther, Nucl. Phys. A 333 (1980) 381.
[50] S. Galster, H. Klein, J. Moritz, K.H. Schmidt, D. Wegener, J. Bleckwenn, Nucl. Phys. B 32 (1971) 221.
[51] H. Chandra, G. Sauer, Phys. Rev. C 13 (1976) 245.
[52] G.R. Satchler, Nucl. Phys. A 472 (1987) 215.
[53] A. Krasznahorkay, H. Akimune, A.M. van den Berg, N. Blasi, S. Brandenburg, M. Csatlos, M. Fujiwara, J. Gulyas, M.N. Harakeh, M. Hunyadi, M. de Huu, Z. Mate, D. Sohler, S.Y. van der Werf, H.J. Wörtche, L. Zolnai, Nucl. Phys. A 731 (2004) 224.
[54] K. Langanke, G. Martinez-Pinedo, P. von Neumann-Cosel, A. Richter, Phys. Rev. Lett. 93 (2004) 202501.
[55] U. Zurmühl, P. Rullhusen, F. Smend, M. Schumacher, H.G. Börner, S.A. Kerr, Phys. Lett. B 114 (1982) 99;
U. Zurmühl, P. Rullhusen, F. Smend, M. Schumacher, H.G. Börner, S.A. Kerr, Z. Phys. A 314 (1983) 171.
[56] N. Tsoneva, H. Lenske, Prog. Part. Nucl. Phys. 59 (2007) 317.
[57] S. Goriely, Phys. Lett. B 460 (1998) 136.
[58] J.J. Cowan, F.-K. Thielemann, J.W. Truran, Phys. Rep. 208 (1991) 267.
[59] Th. Weber, R.D. Heil, U. Kneissl, W. Wilke, Th. Kihm, K.T. Knöpfle, H.J. Emrich, Nucl. Phys. A 510 (1990) 1.
[60] P.K.A. de Witt Huberts, J. Phys. G 16 (1990) 507.
[61] J. Wesseling, C.W. de Jager, L. Lapikas, H. de Vries, M.N. Harakeh, N. Kalantar-Nayestanaki, L.W. Fagg, R.A. Lindgren, D. Van Neck, Nucl. Phys. A 547 (1992) 519.
[62] G.J. Kramer, H.P. Blok, L. Lapikas, Nucl. Phys. A 679 (2001) 267.
[63] D. Van Neck, M. Waroquier, J. Ryckebusch, Nucl. Phys. A 530 (1991) 347.
[64] V.R. Pandharipande, I. Sick, P.K.A. de Witt Huberts, Rev. Mod. Phys. 69 (1997) 981.
[65] T. Otsuka, T. Suzuki, R. Fujimoto, H. Grawe, Y. Akaishi, Phys. Rev. Lett. 95 (2005) 232502.
[66] O. Benhar, D. Day, I. Sick, Rev. Mod. Phys. 80 (2008) 189.
[67] C. Barbieri, D. Rohe, I. Sick, L. Lapikas, Phys. Lett. B 608 (2005) 47.
[68] D. Rohe, A1 and A3 collaboration, Eur. Phys. J. A 28 (2006) 29.
[69] J.D. Bjorken, S.K. Mtingwa, Part. Acceler. 13 (1983) 115.
[70] E.L. Saldin, E.A. Schneidmiller, M.V. Yurkov, Nucl. Instr. and Meth. A 375 (1996) 336.
[71] M.V. Ricciardi, S. Lukić, A. Kelić, K.-H. Schmidt, M. Veselsky, Eur. Phys. J. Spec. Top. 150 (2007) 321.
[72] H. Geissel, H. Weick, M. Winkler, G. Münzenberg, V. Chichkine, M. Yavor, T. Aumann, K.H. Behr, M. Böhmer, A. Brünle, K. Burkard, J. Benlliure, D. Cortina-Gil, L. Chulkov, A. Dael, J.-E. Ducret, H. Emling, B. Franczak, J. Friese, B. Gastineau, J. Gerl, R. Gernhäuser, M. Hellström, B. Jonson, J. Kojouharova, R. Kulessa, B. Kindler, N. Kurz, B. Lommel, W. Mittig, G. Moritz, C. Mühle, J.A. Nolen, G. Nyman, P. Roussell-Chomaz, C. Scheidenberger, K.-H. Schmidt, G. Schrieder, B.M. Sherrill, H. Simon, K. Sümmerer, N.A. Tahir, V. Vysotsky, H. Wollnik, A.F. Zeller, Nucl. Instr. and Meth. B 204 (2003) 71.
[73] K.-H. Schmidt, E. Hanelt, H. Geissel, G. Münzenberg, J.P. Dufour, Nucl. Instr. and Meth. A 260 (1987) 287.
[74] C.J. Benesh, B.C. Cook, J.P. Vary, Phys. Rev. C 40 (1998) 1198.
[75] C. Scheidenberger, H. Geissel, H.H. Mikkelsen, F. Nickel, T. Brohm, H. Folger, H. Irnich, A. Magel, M.F. Mohar, G. Münzenberg, M. Pfützner, E. Roeckl, I. Schall, D. Schardt, K.-H. Schmidt, W. Schwab, M. Steiner, Th. Stöhlker, K. Sümmerer, D.J. Vieira, B. Voss, M. Weber, Phys. Rev. Lett. 73 (1994) 50;
C. Scheidenberger, H. Geissel, H.H. Mikkelsen, F. Nickel, S. Czajkowski, H. Folger, H. Irnich, G. Münzenberg, W. Schwab, Th. Stöhlker, T. Suzuki, B. Voss, Phys. Rev. Lett. 77 (1996) 3987;
N. Iwasa, H. Geissel, G. Münzenberg, C. Scheidenberger, Th. Schwab, H. Wollnik, Nucl. Instr. and Meth. B 126 (1997) 284.
[76] S.Y.F. Chu, L.P. Ekström, R.B. Firestone. The Lund/LBNL Nuclear Data Search Version 2.0, February, 1999 〈http://nucleardata.nuclear.lu.se/nucleardata/toi/listnuc.asp?sql=&A1=1&A2=238〉.
[77] M. Steck, C. Dimopoulou, A. Dolinskii, F. Nolden, Proceedings of PAC07, Albuquerque, New Mexico, USA, 2007, p. 1425.
[78] J. Eichler, Th. Stöhlker, Phys. Rep. 439 (2007) 1.
[79] Th. Stöhlker, T. Ludziejewski, H. Reich, F. Bosch, R.W. Dunford, J. Eichler, B. Franzke, C. Kozhuharov, G. Menzel, P.H. Mokler, F. Nolden, P. Rymuza, Z. Stachura, M. Steck, P. Swiat, A. Warczak, T. Winkler, Phys. Rev. A 58 (1998) 2043.
[80] J. Eichler, Th. Stöhlker, Hyperfine Int. 114 (1998) 277.
[81] MEFIT B. Dreher, K. Merle, MEFCAL, University of Mainz, unpublished.
[82] H. Diesener, U. Helm, G. Herbert, V. Huck, P. von Neumann-Cosel, C. Rangacharyulu, A. Richter, G. Schrieder, A. Stascheck, A. Stiller, J. Ryckebusch, J. Carter, Phys. Rev. Lett. 72 (1994) 1994;
H. Diesener, U. Helm, P. von Neumann-Cosel, A. Richter, G. Schrieder, A. Stascheck, A. Stiller, J. Carter, Nucl. Phys. A 696 (2001) 272.
[83] K.I. Blomqvist, W.U. Boeglin, R. Böhm, M. Distler, R. Edelhoff, J. Friedrich, R. Geiges, P. Jennewein, M. Kahrau, M. Korn, H. Kramer, K.W. Krygier,

V. Kunde, A. Liesenfeld, H. Merkel, K. Merle, U. Müller, R. Neuhausen, E.A.J.M. Offermann, Th. Pospischil, A.W. Richter, G. Rosner, P. Sauer, S. Schardt, H. Schmieden, A. Wagner, Th. Walcher, S. Wolf, Nucl. Instr. and Meth. A 403 (1998) 263.
[84] W. Brooks, CLAS Collaboration, Nucl. Phys. A 663 (2000) 1077.
[85] J. Friese, for the HADES collaboration, Nucl. Phys. A 654 (1999) 1017c.
[86] The BLAST Collaboration, Technical Design Report, 1997 ⟨http://blast.lns.mit.edu/BlastNotes/⟩; R. Alarcon and BLAST Collaboration, Nucl. Phys. A663 (2000) 1111.
[87] The BELLE Collaboration, KEK Progress Report 2000-4 ⟨http://beauty.bk.tsukuba.ac.jp/belle/nim/⟩; Nucl. Instr. and Meth. A479 (2002) 117.
[88] International Workshop on Rare Isotope Physics at Storage Rings, 2002, Hirschegg, Austria ⟨http://www-win.gsi.de/frs/meetings/hirschegg/Talks/Thursday/Blomquist.pdf⟩; ⟨http://www-win.gsi.de/frs/meetings/hirschegg/Talks/Thursday/Kato.pdf⟩.
[89] V. Bondarenko, B. Dolgoshein, V. Grigoriev, O. Kondratiev, A. Medvedev, S. Pavlenko, M. Potekhin, A. Romaniouk, V. Sosnovtsev, V. Tcherniatine, S. Muraviev, Nucl. Instr. and Meth. A 327 (1993) 386.
[90] J.V. Allaby, W. W Ash, H.R. Band, L.A. Baksay, H.T. Blume, M. Bosman, T. Camporesi, G.B. Chadwick, S.H. Clearwater, R.W. Coombes, M.C. Delfino, R. de Sangro, W.L. Faissler, E. Fernández, W.T. Ford, M.W. Gettner, G.P. Goderre, Y. Goldschmidt-Clermont, B. Gottschalk, D.E. Groom, B.K. Heltsley, R.B. Hurst, J.R. Johnson, H.S. Kaye, K.H. Lau, T.L. Lavine, H.Y. Lee, R.E. Leedy, S.P. Leung, I. Lippi, E.C. Loh, H.L. Lynch, A. Marini, J.S. Marsh, T. Maruyama, R.L. Messner, O.A. Mayer, S.J. Michalowski, S. Morcos, J.H. Moromisato, R.M. Morse, L.J. Moss, F. Muller, H.N. Nelson, I. Peruzzi, M. Piccolo, R. Prepost, J. Pyrlik, N. Qi, A.L. Read Jr., K. Rich, D.M. Ritson, F. Ronga, L.J. Rosenberg, W.D. Shambroom, J.C. Sleeman, J.G. Smith, J.P. Venuti, P.G. Verdini, E. von Goeler, H.B. Wald, R. Weinstein, D.E. Wiser, R.W. Zdarko, Nucl. Instr. and Meth. A 281 (1989) 291.
[91] A1 collaboration ⟨http://wwwa1.kph.uni-mainz.de/A1/vdc.html⟩.
[92] V. Kouznetsov, A. Lapik, S. Churikova, B. Girolami, D. Karapetiantz, Yu. Malyukin, V. Nedorezov, A. Turinge, Yu. Vorobiev, V. Abramov, A. D'Angelo, D. Moricciani, L. Nicoletti, Yu. Ranyuk, C. Schaerf, Nucl. Instr.and Meth. A 487 (2002) 396.
[93] H.W. Koch, J.W. Motz, Rev. Mod. Phys. 31 (1959) 920.
[94] C.J. Bocchetta, A. Wrulich, Nucl. Instr. and Meth. 278 (1989) 807.
[95] K. Mengel, R. Novotny, W. Doring, V. Metag, R. Beck, H. Ströher, IEEE Trans. Nucl. Sci. NS-45 (1998) 681.
[96] A.S. Brogna, S. Buzzetti, W. Dabrowski, T. Fiutowski, B. Gebauer, M. Klein, C.J. Schmidt, H.K. Soltveit, R. Szczygiel, U. Trunk, Nucl. Instr. and Meth. A 568 (2006) 301.
[97] H.G. Essel, J. Hoffmann, N. Kurz, R.S. Mayer, W. Ott, D. Schall, IEEE Trans. Nucl. Sci. NS-43 (1996) 132;
H.G. Essel, N. Kurz, IEEE Trans. Nucl. Sci. NS-47 (2000) 337.
[98] Synergy Group for Front-End Electronics, Data Acquisition and Controls (SGFDC) ⟨http://www.gsi.de/fair/experiments/NUSTAR/WGs/FEE-DAQ/⟩.
[99] H.H. Gutbrod, I. Augustin, H. Eickhoff, K.-D. Groß, W.F. Henning, D. Krämer, G. Walter (Eds.), FAIR Baseline Technical Report, 2006 ⟨http://www.gsi.de/fair/reports/btr.html⟩.